Cape Peninsula University of Technology

NUMERICAL AND EXPERIMENTAL INVESTIGATION OF DIRECTIONAL SOLIDIFICATION IN VACUUM INVESTMENT CASTING OF SUPERALLOYS

EKATERINA RZYANKINA

Thesis submitted in fulfilment of the requirements for the degree
Master of Technology: Mechanical Engineering
in the Faculty of Engineering
at the Cape Peninsula University of Technology

Supervisor: **Dr Nawaz Mahomed**

Co-supervisor: **Dr inz. Andrzej Nowotnik**

June 2013

DECLARATION

I, Ekaterina Rzyankina, declare that the contents of this dissertation/thesis represent my own unaided work, and that the dissertation/thesis has not been previously submitted for academic examination towards any qualification. Furthermore, it represents my own opinions and not necessarily those of the Cape Peninsula University of Technology.

_____   _____
Signed   **Date**

ABSTRACT

High temperatures encountered in combustion chambers of jet engines has demanded the creation of new technologies and new materials for the construction of one of the most critical elements of these systems - the stator and rotor turbine blades. They have to withstand extreme temperatures for extended periods without the loss of mechanical strength, conditions under which many steels and alloys fail. Such failure is ascribed to the combination of high temperatures and high centrifugal forces, resulting in creep.

The high temperature creep mechanism of grain boundary sliding has limited the operation capability of fine-grained equiaxed castings. Higher operating temperatures were achieved with higher alloy contents and coarse-grained equiaxed castings. This is especially prevalent in multi-crystalline structures in which grain boundaries present weaknesses in the structure. However, notwithstanding these improvements, high temperature resistant alloys formed as single crystal structures offer the necessary material properties for safe performance under these extreme conditions.

Damage to turbine blade surfaces is often caused by oxidation and hot corrosion. For this reason, turbine blades are coated with a thermal barrier coating (TBC), which consists of ceramic materials that reduce the heat flux through the airfoil.

In this research work, modelling and simulation techniques were initially used to study the directional solidification (DS) of crystal structures during vacuum investment casting. The modelling of the solidification process was implemented using a Finite Element casting simulation software, ProCAST, to predict thermal and flow profiles.

These models allowed the study of the dendritic growth rate, the formation of new grains ahead of the solid/liquid interface and the morphology of the dendritic microstructure. These studies indicated the opportunity to optimise the velocity of the solidification front (solidification rate) for single crystal structures.

The aim of this research was therefore to investigate the effect of the solidification rate (or withdrawal velocity) on the quality of SC castings. The investigations were carried out for nickel-based superalloy CMSX-4 turbine blade casts and rods using the Bridgman process for vacuum investment casting. The SC castings were heat treated to improve the grain structure for enhanced creep resistance. The heat treated SC castings were inspected by X-ray diffraction to analyse crystallographic orientation and chemical composition; and by SEM,

OP (optical microscopy) and microprobe analysis to analyse the microstructure; in addition to macrostructural investigations.

In the experimental analysis, the formation of new grains ahead of the solidi/liquid interface and the effect of dendrite packing patterns on the primary dendrite spacing were investigated.

Creep tests were conducted to compare the creep properties of the SC castings for different withdrawal rates, and to draw conclusions regarding the effect of withdrawal rate on the microstructure (and hence the creep properties) of SC castings.

ACKNOWLEDGEMENTS

I wish to thank:

- Dr Nawaz Mahomed - my supervisor; my sincere gratitude to him. Apart from his high standard of supervision, he has given me painstaking guidance on my MTech study. He has also provided me with precious opportunities to collaborate with other institutions and to present my work at conferences, which were very beneficial for me, not only for my MTech research, but also for my future career. His help and motivation has certainly provided a huge contribution towards the completion of a successful project.
- Dr inz. Andrzej Nowotnik for his expert and valuable guidance and support throughout my experimental research.
- M inz. Dariusz Szeliga for his help with many practical aspects, in particular the casting experiments and the simulations in ProCAST.
- Prof Graeme Oliver for his guidance and support.
- S.A. Rzyankin, Z.G. Rzyankina - my deepest appreciation and warmest regards to my dear parents for their endless love.
- M.N. Abrahams - he has given me encouragement in all situations.
- All the technicians at the Research and Development Laboratory for Aerospace Materials involved in this project – their support is highly appreciated.

DEDICATION

This thesis is dedicated to my parents

Sergey A. Rzyankin, Zulfiya G. Rzyankina

GLOSSARY

DS   - directional solidification

SC   - single crystal

EC   - equiaxed crystal

CC   - conventional cast

HABs   - high of angle boundaries

CET   - columnar to equiaxed transition

TBC   - thermal barrier coating

FCC   - face centred cubic

TCP   - topologically close-packed

CVD   - chemical vapour deposition

PLMCC   - Product Lifecycle Management Competency Centre

EB-PVD   - electron beam - physical vapour deposition

AC   - air cooling

GFQ   - gas furnace quench

SEM   - scanning electron microscopy

OP   - optical microscopy

KGT   - Kurz-Giovanola-Trivedi model

CAFE   - cellular automaton finite element

CAD   - computer aided design

EFG   - electric field gradient

LMC   - liquid-metal coolant

PDA   - primary dendrite arm

SDA   - secondary dendrite arm

TCP   -topological close-packed

TABLE CONTENTS

LIST OF FIGURES

LIST OF TABLES

CHAPTER ONE: INTRODUCTION

1.1 Background

Special technological and metallurgical properties of high performance components in the aircraft industry have been obtained through manufacturing techniques, such as directionally solidified (DS) casting techniques followed by single crystal (SC) techniques, the latter in particular for turbine blade manufacture.

Vacuum investment casting is used to produce complex-shaped turbine blades, required by designers to obtain improved performance of jet engines. Modern processes of design and manufacture of DS and SC castings have become significantly reliant on modelling and simulation of the casting process in order to produce defect-free turbine blades. In essence, the main features of high-performance gas turbine blades are: good high-temperature creep, corrosion and oxidation resistance, high-cycle fatigue resistance and microstructural stability.

All these performance characteristics can be achieved through the use of high-temperature alloys, also known as superalloys, coupled with a strict control of casting parameters in relation to the grain size and growth direction during solidification, resulting in columnar-grained or single-grained structure. The latter implied that there no grain boundaries, and is also referred to as single crystal structures.

The final metal structure and thermo-mechanical properties are dependent on the (casting) process parameters and on the thermal gradients during solidification (Galantucci 1998:160).

1.2 Awareness of the Problem

One of the major challenges facing the South African metal casting industry is the production of high performance superalloy components from high quality ingots for power generation and aerospace applications. The technology required for the identification of the process variables that are important for high quality single crystal turbine blade production, in particular, has not been successfully localised. This includes the capability to simulate the industrial processes to optimise the production process variables as well as experience in the actual production technologies associated with single crystal growth of nickel-based alloy castings.

An important application of superalloys is the production of turbine blades. The grain boundaries represent structural weaknesses, and the performance of these components

could be significantly improved by directional or single crystal solidification. The progress in superalloy performance would not have been possible without the parallel development of prosessing technologies. The use of vacuum induction melting enabled the control of undesirable residual elements and non-metallic inclusions.

1.3   Problem Statement

The primary goal of this research work was to accurately model the casting solidification of single crystal turbine blades in order to more clearly understand the growth of the dendritic crystal structure and to optimise the crystal growth parameters.

The research aims to initially use modelling and simulation methods to simulate and optimise the growth parameters and defect formation in vacuum investment casting of high performance single crystal turbine blade. Thereafter, experimental casting analysis will be carried out to validate the simulation results. Hence, the theory of solidification of single crystal castings, numerical simulation and experimental analysis will be used in conjunction with each other for the vacuum investment casting investigation of single crystal turbine blades.

1.4   Facilities

The Foundry Technology Research Group in the Faculty of Engineering at CPUT is a relatively new development, and focuses on the mechanics of solidification and numerical optimisation of casting processes. The software, Magmasoft, is available for the computational simulation of metal casting processes. Together with the Product Lifecycle Management Competency Centre, the development of accurate geometric models, through the use of CATIA, can be accomplished prior to process simulation.

The Research and Development Laboratory for Aerospace Materials at Rzeszow University of Technology was started in 2005 through funding from the Ministry of Education and Science and the European Union. This facility is affiliated to the Rzeszow University of Technology's Department of Materials Science and uses the research capacity of the universities consortium within the AERONET-Aviation Valley Centre of Advanced Technologies and the CAMAT Centre of Advanced Materials and Technologies, as well as a group of engineers working in the Aviation Valley aerospace cluster.

The Laboratory for Aerospace Materials includes an industrial-strength laboratory vacuum furnace for directional crystallisation of high-temperature creep resistant alloys, equipment for producing high-temperature protective coatings by chemical vapour deposition (CVD) and advanced technology for thermal barrier coatings for turbine blades & vanes: such as

LPPS thin film for MCrAlY & YSZ plasma spraying, and electron beam physical vapour deposition for YSZ deposition (EB-PVD). It also has ProCast simulation software for simulating vacuum investment casting processes.

1.5   Nickel-based Superalloys

The term "Superalloys" refers to a specific class of materials which is difficult to delineate. Superalloys, which have made much of today's very high temperature engineering technology possible, are the materials leading edge of the turbines that drive jet engines (Campbell, 2000:45).

Nickel-based superalloys are capable of being used in load-bearing applications in excess of 80% of their incipient melting temperatures, display good corrosion resistance, and have the ability operate at elevated temperatures for extended periods of time. They can operate at temperatures exceeding 1000^{0}C.   Originally, turbine blades were made from conventional wrought materials in the form of forgings (Campbell, 2006:200).

However, the high temperature creep mechanism of grain boundary sliding limited the operating capability of these fine-grained equiaxed structures.   Higher operating temperatures were achieved with higher alloy contents and coarse equiaxed grain castings. Even further improvements were made with DS castings, which eliminated the transverse grain boundaries. Finally, SC casting technology was developed that eliminated all the grain boundaries. The development of SC castings also allowed alloy designers to remove alloying elements that were added to prevent grain boundary cracking but were detrimental to creep strength.

The Edisonian experimenters of the 1930s succeeded in creating strong alloys, built on the austenitic nickel-bases solid solution containing chromium (called γ). Jet engine turbine blades are mostly made from Ni-based superalloys.   The development of superalloys allowed the industry to have superior mechanical properties: strength, creep and oxidation resistance at elevated temperatures. Compared with other alloys, Ni-based superalloys provide the best durability and strength at high temperatures, especially with operating temperatures above $800\,^{0}$C.

The high temperature properties of Ni-based superalloys arise from:
(a) Ni has a face centred cubic (FCC) crystal structure with high melting point, which makes it ductile and tough;

(b) Ni is stable in the FCC crystal structure from room temperature to its melting point. Therefore, no phase transformations will occur that will cause expansions and contractions which might complicate its use in high-temperature components; and

(c) Diffusion rates in Ni are low which impart considerable microstructure stability at elevated temperatures and high creep resistance (Reed, 2006:3).
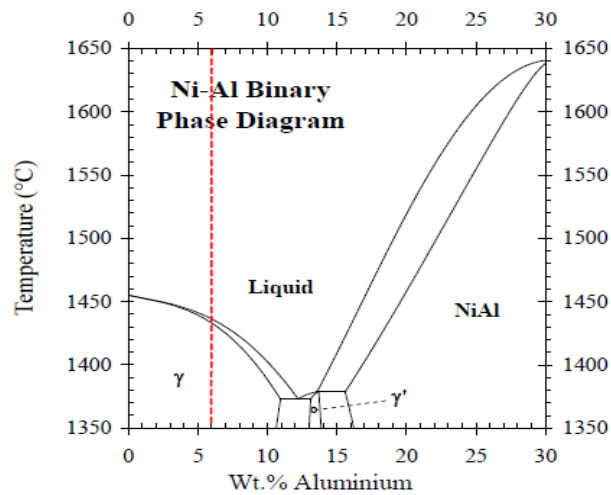
Figure 1.1: The Ni-Al binary phase diagram (Calculated by Henrik Larsson using Thermo-CalcTM).

The red dashed line indicates the alloy with 6 wt. % Al. At room temperature there are two phases, γ and γ', in the system.
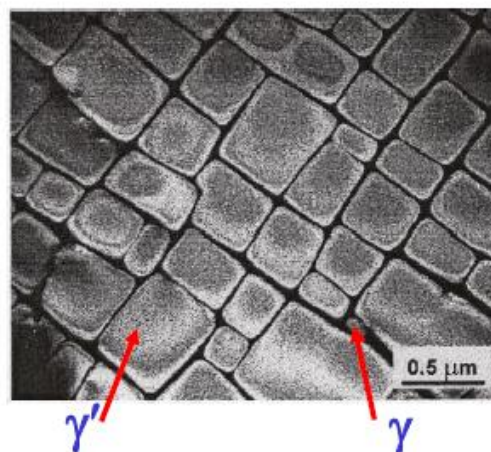
Figure 1.2: The microstructure of γ and γ' phases is illustrated (Adapted from Caron and Khan, 1999).

1.6   Chemistry of Ni-based alloys of Turbine Blades

Ni-based superalloys are complex alloy systems constituted of more than ten alloying elements. The chemical modification from conventional cast alloys to the up-to-date single crystal superalloys of the fourth generation is listed in Table 1 (Reed, 2006:22).

Table 1.1: Chemical composition from conventional cast (CC) alloys to the 4th generation single crystal superalloys (wt.%, bal. Ni)

Alloy	Cr	Co	Mo	W	Ta	Re	Nb	Al	Ti	Hf	C	B	Y	Zr	Ru
Conventional Cast Alloys															
Mar–M246	8.3	10.0	0.7	10.0	3.0			5.5	1.0	1.5	0.14	0.02		0.05	
IN 100	10.0	15.0	3.0					5.5	4.7		0.18	0.01		0.06	
Rene 80	14.0	9.5	4.0	4.0				3.0	5.0		0.17	0.02		0.03	
Directionally Solidified alloys															
IN 792	12.6	9.0	1.9	4.3	4.3			3.4	4.0	1.00	0.09	0.02		0.06	
GTD 111	14.0	9.5	1.5	3.8	2.8			3.0	4.9		0.10	0.01			
1th Generation SX Alloys															
PWA 1480	10.0	5.0		4.0	12.0			5.0	1.5						
Rene N4	9.8	7.5	1.5	6.0	4.8		0.5	4.2	3.5	0.15	0.05				
CMSX-3	8.0	5.0	0.6	8.0	6.0			5.6	1.0	0.10					
2nd Generation SX Alloys															
PWA1484	5.0	10.0	2.0	6.0	9.0	3.0		5.6		0.10					
Rene N5	7.0	7.5	1.5	5.0	6.5	3.0		6.2		0.15	0.05		0.01		
CMSX-4	6.5	9.0	0.6	6.0	6.5	3.0		5.6	1.0	0.10					
3rd Generation SX Alloys															
Rene N6	4.2	12.5	1.4	6.0	7.2	5.4		5.8		0.15	0.05		0.01		
CMSX-10	2.0	3.0	0.4	0.5	8.0	6.0	0.1	5.7	0.2	0.03					
4th Generation SX Alloys															
MC-NG	4.0	0.2	1.0	5.0	5.0	4.0		6.0	0.5	0.1					4.0
RR2101	2.5	12		9.0	5.5	6.4		6.0		0.15					2.0

The performance of 2nd and 3rd generation SC superalloys has been significantly improved by the addition of increasing amounts of Re element (3 wt. % and 6 wt. % respectively). The 4th generation SC superalloys are developed by adding Ru to boost structural stability, resulting in the development of MC-NG and RR2101 alloys.
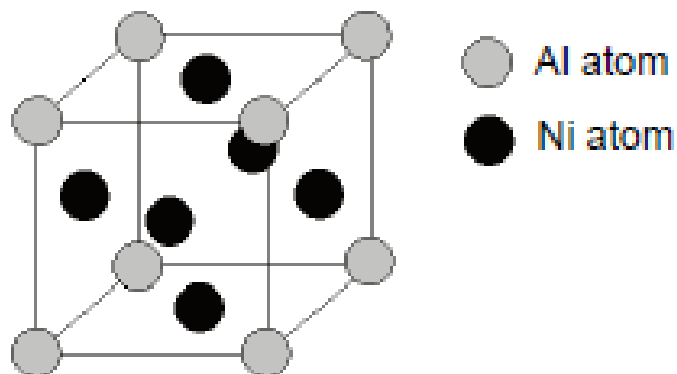
Figure 1.3: Crystal structure the γ' phase Ni superalloys

The cube-cube relationship makes the cell edges of these two phases exactly parallel, and the similar lattice parameters make the γ' phase coherent with the γ phase when the precipitate size is small. The coherent γ' phase strengthens the alloy by interfering with dislocation motion. Furthermore, the small misfit between γ and γ' lattices contributes to the change of microstructure under the influence of the stress at elevated temperatures positively to the stability of the microstructure (Hillier et al. 1988: 45).

The amount of γ' phase and the misfit between γ and γ' lattices can be controlled by altering the chemical composition and the processing conditions.

CMSX-4 consists of the following composition:

Al: promotes the creation of the γ' phase and plays a fundamental role in promoting the formation of a stable Al_2O_3 alumina surface scale, which protects the alloy against further oxidation.

Cr: acts as a solid solution strengthening element and plays an essential role in the hot corrosion and oxidation resistance. Cr also forms the topologically close-packed brittle phase (TCP), and the TCP phase is detrimental to high temperature properties of the turbine blades.

Co: contributes to the strength by ordering γ' phase particles homogeneously distributed in the γ matrix.

Mo: strengthens the γ/γ' phases, but has a negative influence on the corrosion resistance of Ni-based superalloys.

W: improves high temperature capability, segregates strongly to the γ dendrites and increases the potential for nucleation and growth of grain defects at high levels of W.

Ta: strengthens the γ' precipitates by substituting for Al in γ', particularly increasing high-temperature strength. Ta segregates to the interdendritic region, so can decrease the density inversions which will cause the nucleation of spurious grains. Ta is also beneficial for environmental properties.

Re: improves high temperature capability, hot corrosion and oxidation resistance at the expense of density and microstructure stability. Re has played a key role in the evolution of single crystal superalloys.

Nf, Ti: strengthen the γ' precipitates by substituting for Al in γ', particularly increasing high-temperature strength. However, an excessive amount of these elements makes alloys prone to TCP phase precipitation (Durand-Charre, 1997:4).

1.7 Turbine Components and Environment

The components of the hot section of a modern aircraft engine consist of a combustor, rotating and stationary blading. The rotating blades of the turbine, or buckets, convert the kinetic energy of the hot gas exiting the nozzles to shaft horsepower used to drive the compressor and load devices. The blade consists of an airfoil section in the gas path, and a dovetail joint connecting the blade to the turbine disk. Owing to rotation, the blade is subjected to centrifugal stresses. The centrifugal force acting on a unit mass at the blade's mid-span is 13 000–90 000 times that of gravity. Materials development efforts continue on two fronts. Alloys are being modified to enhance resistance to attack, and coatings are being developed which can be applied to protect the bucket alloy from attack. For aircraft engines, similar attention is paid to oxidation (Harold, 2006:780).

Blade material requirements include corrosion and excitation resistance or the existence of a good protective coating system, in addition to fatigue and creep strength.
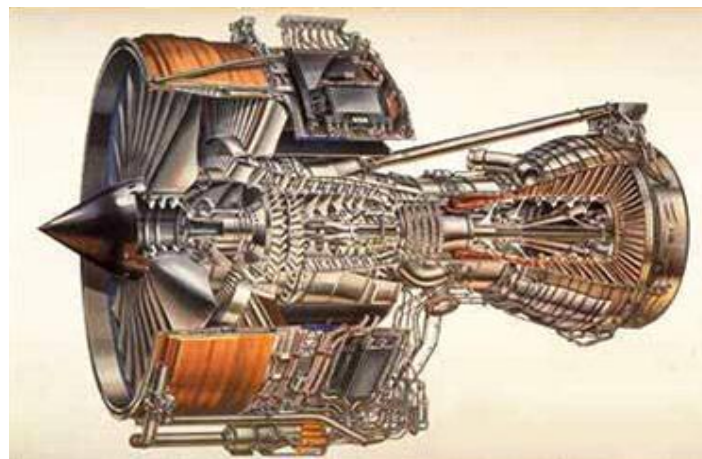
Figure 1.4: Rolls-Royce Trent 800 aero engine (Adapted from Rolls –Royce).

1.8 Research Objectives

The main objective of the research is the study and verification of the processes for precision casting (vacuum investment casting) of the major elements of aircraft engine turbines (including the turbine blades) made from superalloys (nickel-based) with a single crystal structure with directionally oriented grains [001]. This will require, as a precursor to experimental verification, the development of the (theoretical) conditions for the manufacture of single crystal turbine blades, using well-established solidification theory. The optimisation of the investment casting process will be carried out using different withdrawal velocities (or solidification rates) using simulation modelling ProCAST software. Thereafter, three casting experiments, including heat treatment, will be analysed for microstructural (OP, SEM), macrostructural, diffraction analysis of crystal structure and mechanical properties.

CHAPTER TWO: ANALYSIS OF DIRECTIONAL AND SINGLE CRYSTAL SOLIDIFICATION

2.1 DS and SC Superalloys

Directionally solidified and single crystal superalloys have the highest elevated temperature capability of any material. There are two primary reasons that explain why DS superalloys are superior compared with conventionally cast (CC) superalloys.

One of the benefits of the directional solidification process is that it removes grain boundaries which can be the site of failure where cracks initiate. This is especially useful in eliminating grain boundaries normal to the axis of applied stress. Also directional solidification can be used to produce a [001] crystal which is aligned with the loading directional which improves thermal fatigue resistance. The DS superalloy can be heat treated to reduce precipitates which will prevent segregation after casting.

2.2 Microstructure Evolution during the Casting Process

The microstructure of DS and SC superalloys is similar to CC superalloys consisting primarily of γ' precipitate particles in γ Ni matrix with a few carbides and borides. The microstructure of a casting is important since many material properties, especially mechanical properties, depend on the grain shape and size. Furthermore, segregation resulting from solute partitioning during solidification can have significant effects.
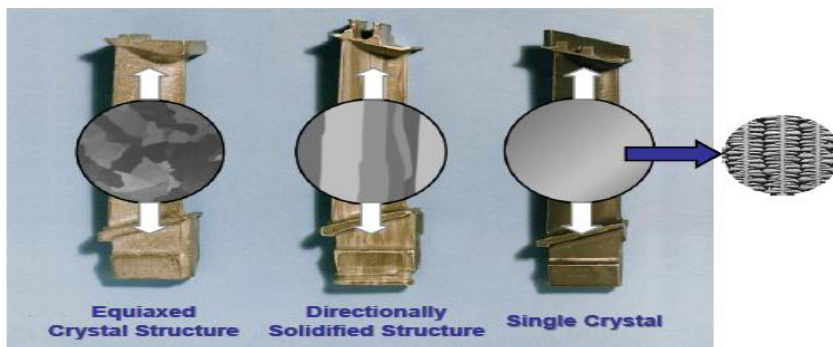
Figure 2.1: The microstructure of turbine blade (Adapted from H.B Dong, 2007:4)

2.3 Dendritic Structure

The first appearance of a solid in the melted metal is referred to as the nucleus. As the solid grows, the spherical morphology eventually becomes unstable, which leads to formation of dendrites. The dendrite consisting of a primary trunk growing along one of the six equivalent [001] directions of the crystal, with secondary arms in the four conjugate [001] directions appearing just behind the advancing dendrite tip (Dantzig, Rappaz 2009:196).

Dendrites are the most prevalent structure in casting alloys, and the pattern of dendrites determines the final properties of castings (Hunt 1984; Pollock et al. 1992; Kurz and Fisher, 1984). Generally, two distinct forms of dendritic structures, columnar and equiaxed dendrites, exist in castings. The structure is called columnar if the growth is preferentially oriented in a direction close to the heat flux, whereas equiaxed grains are growing in all directions, leading to a material with more isotropic macroscopic mechanical properties and a more homogeneous composition than those with columnar microstructure (Mirihanage et al. 2013:218).

2.4   Columnar to Equiaxed Transition (CET)

The crystal grains can be columnar or equiaxed, and are the result of mechanisms of nucleation and growth of the primary phase solidified in a thermal gradient. Transition from columnar grain structure to equiaxed grain structure can be observed (Figure 2.2). As solidification progressed, the increasing pulling velocity led to a rise of the tip undercooling ahead of the columnar dendrites and therefore offered more chance for the heterogeneous nuclei to form. Quicker growth of the new grains into the equiaxed shape is as a result of the equiaxed grains forming ahead of the columnar front which had greater constitutional undercooling than the existing columnar dendrites. Some of the equiaxed grains will overgrow the columnar dendrites and the columnar-to-equiaxed transition (CET) occurred.
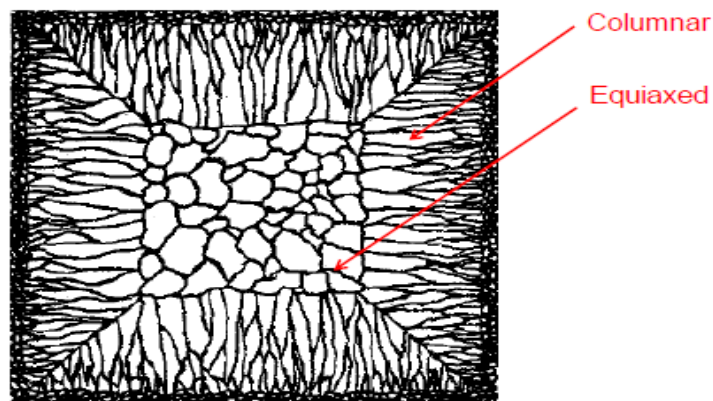
Figure 2.2: Columnar-to-equiaxed transition (CET) (Adapted from Campbell, 2003:124).

2.5   Primary Spacing in Dendrites

As the solid grows, the morphology eventually becomes unstable, which create dendrites. Dendrites have many characteristic such as dendritic tip radius, primary and secondary dendritic arm spacing.
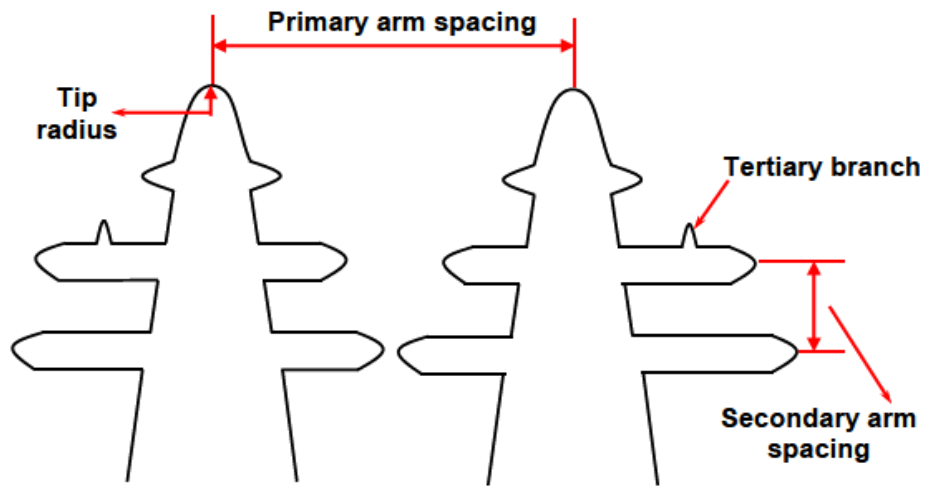
Figure 2.3: Spacing in dendritic structure.

If a member of the dendrite array has a spacing which is too small, it will be overgrown by its neighbours (Figure 2.4 (a)). If the spacing is too large, a new primary dendrite will form by the growth of a tertiary arm (Figure 2.4 (c)).
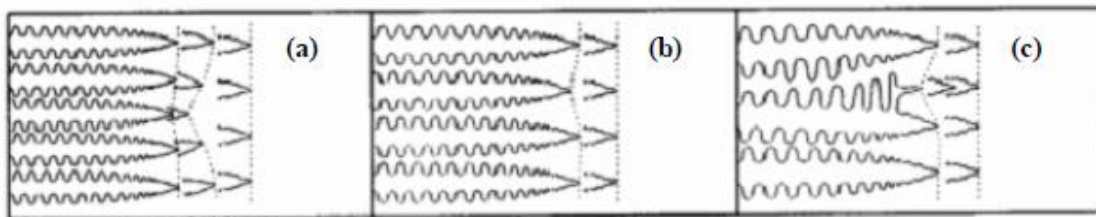
Figure 2.4: A schematic diagram primary spacing for dendrites: a) overgrowth, b) steady state, c) branching (Adapted from Hunt, 1979:78).

2.6   Competitive Growth Model

Since microstructural control during single crystal investment casting depends strongly on the competitive growth of dendrites, understanding the underlying mechanism becomes vital.
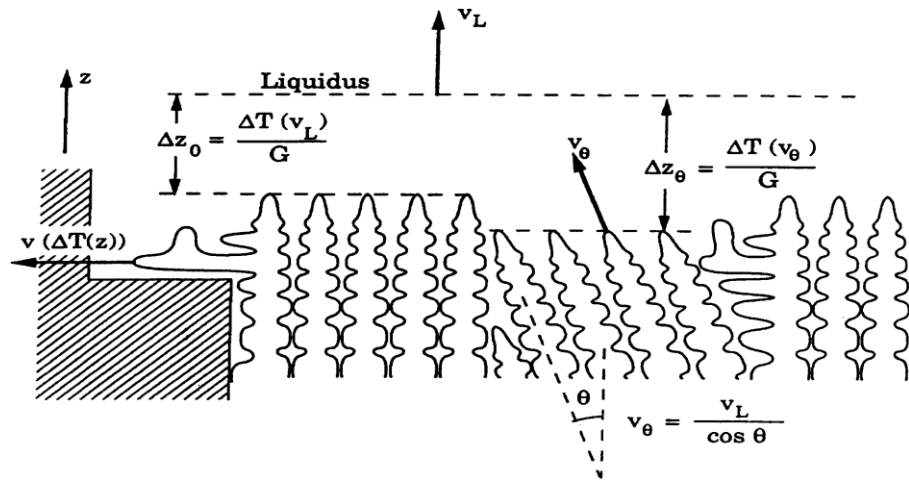
Figure 2.5: The schematics illustration of the competitive growth during solidification
(Adapted from Rappaz and Gandin, 1993:346).

As shown in Figure 2.5, grains on the left and right side contain dendrites with preferred growth direction [001] well aligned with the thermal gradient, and they grow with the same velocity. The grain shown in the middle has a misaligned angle of θ with respect to the direction of the thermal gradient. To keep up with the better aligned neighbours, it must grow with a larger growth rate:

$$V_\theta = \frac{V_L}{cos\theta} \tag{2.1}$$

where V_L= velocity of liquidus isotherm;

θ = misaligned angle to the direction of thermal gradient.

Since the growth rate during solidification is determined by the local tip undercooling (Kurz and Fisher, 1984:68), the misaligned grains in the middle are then characterised by a larger undercooling. This difference in undercooling makes the misaligned grains fall behind and creates the competitive growth mechanism in two situations: converging and diverging.

In a converging case, which is shown on the left in Figure 2.5, it is difficult for the secondary arms to develop from the primary dendrites because of the strong solutal interaction. Since the misaligned grains are behind the well-aligned grains due to the local undercooling, the dendrite tips of misaligned grains will hit the side of well aligned grains and be blocked, generating a grain boundary which is always in the same direction as the growth direction of the well- aligned grains (Rappaz and Gandin, 1993:150).

However, recent experimental analysis on bi-crystal samples during directional solidification shows that the misaligned grain was able to overgrow the well-aligned grain by blocking its primary dendrite chunks by branching at different longitudinal planes (Zhou et al. 2008:56). In a diverging case shown on the right in Figure 2.5, the open space between the two

grains offers the opportunity for the secondary arms of misaligned dendrites to develop, and then the tertiary arms will branch from the secondary arms to adjust the dendrite spacing and to compete with existing other primary dendrite arms during solidification. As a result, the well-aligned grain will eventually overgrow the misaligned grain and generate a grain boundary with an inclined angle which is equal to one third of the angle difference between these two touching grains (Zhou et al. 2008: 36).

2.7 Solidification

Solidification is phase transformation from liquid phase to the solid phase which involves solute diffusion and latent heat (Kurz and Fisher, 1984:25). The process of solidification starts with grain nucleation and continues with grain growth. These phenomena and mechanisms are further discussed in the Sections below.

2.8 Theory of Grain Nucleation

From a thermodynamic point of view, nucleation is the onset of phase transformation. There are two forms of nucleation: homogeneous nucleation and heterogeneous nucleation.

Homogeneous nucleation occurs spontaneously and randomly when there are no preferential nucleation sites by the aid of foreign materials. It involves creation of crystal clusters, each of which has an interface between liquid and solid phases and requires undercooling. Homogeneous nucleation is driven by the change in the Gibbs free energy, ΔG, including the interface term, ΔG_L, and volume term, ΔG_V.

Assuming the nucleus has a spherical shape, ΔG can be written as (Kurz and Fisher, 1984:34):

$$\Delta G = \Delta G_L + \Delta G_V = 4\pi r^2 \sigma - \frac{4\pi r^3}{3}\Delta g \qquad (2.2)$$

where σ = Solid/liquid interface energy,

r = nucleus radius,

ΔG = Gibbs free energy difference between the liquid and solid per unit volume

As shown in Figure 2.5, the nucleus has to exceed a critical radius to be stable. Setting:

$$\frac{d}{dr}(\Delta G) = 0 \qquad (2.3)$$

$$r^0 = -\frac{2\sigma}{\Delta g} \qquad (2.4)$$

where r^0 = critical radius, mm.

The occurrence of homogeneous nucleation is limited to very restricted situations and normally requires a high degree of undercooling. When the melt contains solid particles or is in contact with the mould wall or an oxide layer, nucleation may be facilitated because the activation energy required is decreased. This is known as heterogeneous nucleation (Kurz, Fisher, 1984:34).
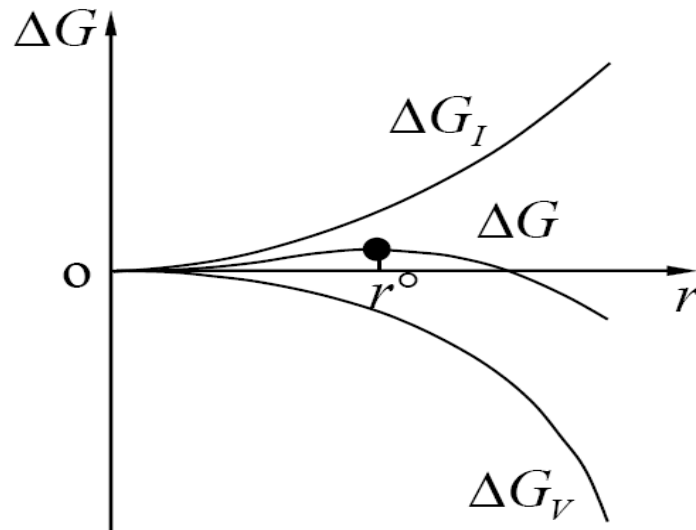
Figure 2.6: Homogenous nucleation (Adapted from Kurz, Fisher 1984:56).

The wetting angle (θ) is defined as the contact angle between the nucleus (crystal) and the foreign solid. The solid/liquid (S/L) interface is partly replaced by the crystal/solid (C/S) interface between the crystal and foreign solid, which has low energy (Figure 2.7). To grow a stable crystal, the energy required for heterogeneous nucleation ΔG_{Het} is given by:

$$\Delta G_{Het} = \Delta G \cdot f(\theta) \tag{2.5}$$

$$f(\theta) = \frac{(2-cos\theta)(1-cos\theta)^2}{4} \leq 1 \tag{2.6}$$

Therefore, activation energy for heterogeneous nucleation is reduced which means heterogeneous nucleation occurs more easily than homogeneous nucleation. Moreover, control of the heterogeneous nucleation can be affected by control of the wetting angle (θ) via selecting appropriate crucible materials or adding appropriate nucleation agents (Dai, 2008:17).
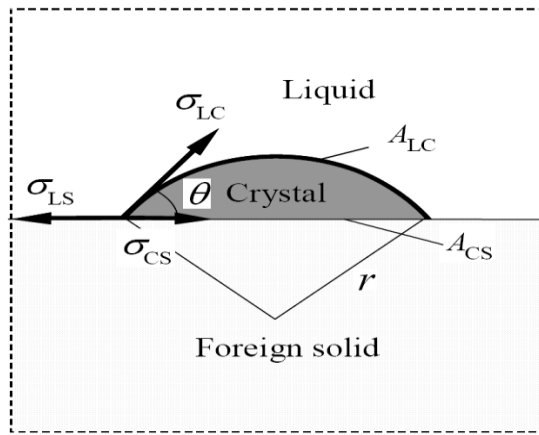
Figure 2.7: Schematic diagram of heterogeneous nucleation
(Adapted from Kurz, Fisher 1984:67).

2.9 Kinetics of Growing Crystals

Once an embryo has grown further than the critical size than what becomes a stable nucleus, kinetics start to dominate the solidification process. This is affected by both solute diffusion and heat transfer in the case of alloys (Dantzing, Rappaz, 2009:423).

2.10 Diffusion

The transformation of liquid into solid is a diffusion controlled process in the absence of convection. The diffusion of both solute and heat need to be considered, which are given by the governing equations:

For solute:

$$\frac{\partial C}{\partial t} = \nabla \cdot (D\nabla C) \tag{2.7}$$

For heat:

$$\frac{\partial T}{\partial t} = \nabla \cdot (\alpha\nabla T) \tag{2.8}$$

$$\alpha = \frac{K}{\rho C_p} \tag{2.9}$$

where D = solute diffusion coefficient for composition C,

α = thermal diffusivity which is defined by Equation 2.6,

K = thermal conductivity,

ρ = density,

C_p= specific heat per unit volume

For binary alloys (k<1), a typical linearized phase diagram is illustrated in Figure 2.9 (Chilton, 2002:56).
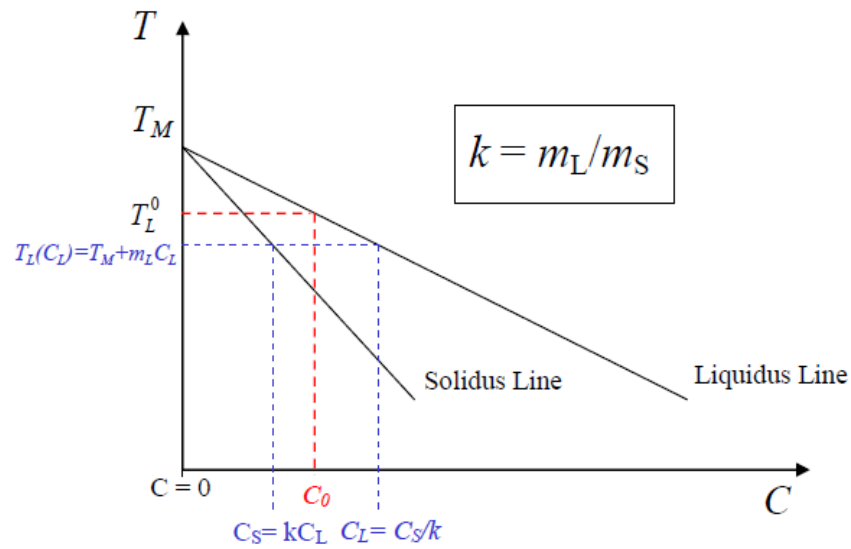
Figure 2.8: Low concentration end of a phase diagram for a typical binary alloy (k<1) (Adapted from Chilton, 2002:78).

The solidus and liquidus are assumed to be approximately straight lines of gradients (m_S) and (m_L). The slopes of liquidus and solidus are (m_L) and (m_S) respectively, the ratio of which is defined as the partition coefficient k:

$$k = \frac{m_L}{m_S} \tag{2.10}$$

which is constant in this case. Therefore, the compositions in the liquid (C_L) and solid (C_S) phases are related by:

$$\frac{\partial C_S}{\partial t} = \nabla \cdot (D_S \nabla C_S) \tag{2.11}$$

$$\frac{\partial C_L}{\partial t} = \nabla \cdot (D_L \nabla C_L) \tag{2.12}$$
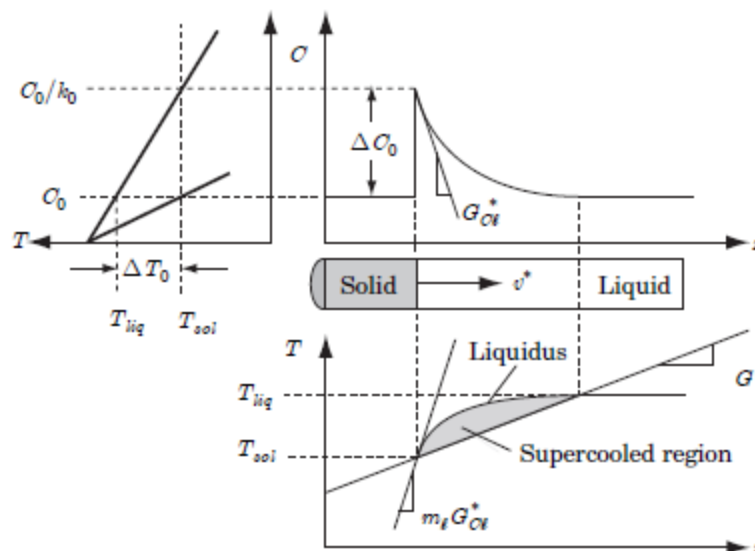
Figure 2.9: Constitutional undercooling (Adapted from J.A Dantzig, M.Rappaz, 2009:304).

16

The constitutional supercooling criterion helped to understand why the planar interface can become unstable during the directional/single crystal solidification of alloys, but reveals nothing about the length scale of the microstructure that develops from instability. A dendrite growing in an undercooling melt can be approximated as a "needle crystal" that is nearly parabolic in shape, except for a small but important correction at the tip, and that grows in a shape-preserving manner at constant velocity.

2.11 Undercooling

During solidification, the local temperature at the solid/liquid (S/L) interface is different from the equilibrium melting temperature of the liquid and the difference is termed as the local undercooling, ΔT. The growth rate and dendrite morphology during solidification is highly dependent on the local undercooling, which has contributions from constitutional undercooling ΔT_C, curvature undercooling, ΔT_R, thermal undercooling, ΔT_t and kinetic undercooling, ΔT_K:

$$\Delta T = \Delta T_C + \Delta T_R + \Delta T_t + \Delta T_K \tag{2.13}$$

Constitutional undercooling due to solute partition and diffusion between solid and liquid is calculated according to:

$$\Delta T_C = m_L(C_\infty - C_L^0) \tag{2.14}$$

where C_∞= bulk alloy composition,

C_L^0= alloy composition at the interface of the liquid,

m_L = liquidus slope

Curvature undercooling refers to the effect of excess energy of the formation of the S/L interface and is determined by:

$$\Delta T_R = K\Gamma \tag{2.15}$$

where Γ= Gibbs-Thomson coefficient,

K = The average curvature at the S/L interface,

$$K = \frac{1}{r_1} + \frac{1}{r_2} \tag{2.16}$$

where r_1 and r_2 are the principal radii of curvature.

The thermal undercooling ΔT_t is related to the release of latent heat and assumes particular significance in pure materials where constitutional undercooling is absent.

The driving force for atoms to transfer from solid to liquid is associated with Kinetic undercooling ΔT_K. The effect of kinetic undercooling is always neglected for metals in terms of the roughness of the S/L interface on the microstructure scale (Chilton, 2002:78).
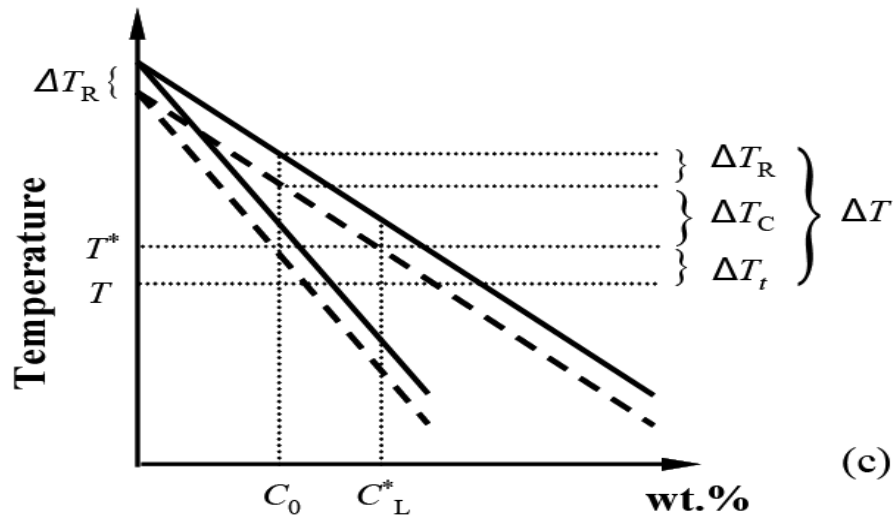
Figure 2.10: The constitutional, curvature and thermal undercooling
(Adapted from Kurz and Fisher, 1984:45).

In pure materials where constitutional undercooling is absent, thermal undercooling ΔT_t is related to the release of latent heat and assumes a particular significance. Kinetic undercooling ΔT_K is associated with the driving force for atoms to transfer from solid to liquid. The effect of kinetic undercooling is always neglected for metals in terms of the roughness of the S/L interface on the microstructure scale (Chilton, 2002:78).
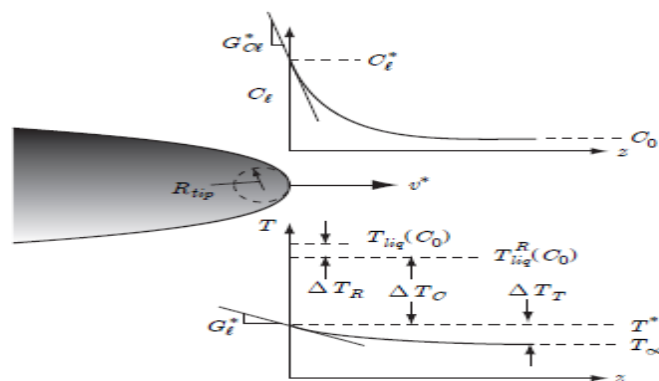
Figure 2.11: Constitutional undercooling for alloys (Adapted from J.A Dantzig, M.Rappaz, 2009:318).

18

2.12 Directional Solidification Single Crystal Process

It is necessary for dendrites (grains) to grow from the one end of the casting to the other to develop a DS solidified structure. This is accomplished by creating a sharp temperature gradient, by removing the majority of the heat from one end of the casting (Campbell, 2006:214).

After the development of the DS casting process, it was recognised that if all but one of the growing columnar grains could be suppressed, it would be possible to cast a part with only a single grain, therefor eliminating all of the grain boundaries. In addition, the alloying elements in casting are necessary to prevent grain boundary cracking and also improve creep strength.

The temperature control and extraction rate are critical. If the extraction rate is too fast, grains will nucleate ahead of the solid/liquid interface, while is the movement is too slow, excessive macrosegregation will occur along with the formation of freckles, which are defects of equiaxed grains of interdendritic composition (Campbell, 2006:213).

Both DS and SC castings are produced via the same basic process. Allowing solidification to occur in a controlled thermal gradient produces elongated grains aligned parallel to the gradient, which, by definition, aligns the grain boundaries parallel to the thermal gradient. DS is accomplished in a vacuum, by pouring molten alloy into a ceramic shell mould that has been preheated to a temperature above the liquidus temperature of the superalloy (Duffy, 1998:4). The preheated shell mould is open at the bottom and sits on a water-cooled copper chill plate. The molten superalloy solidifies upon contact with the copper chill plate to form a thin layer of equiaxed grains. The growth of those grains are mostly closely aligned with the [001] direction parallel to the thermal gradient and produces a columnar array of grains with common vertical [001] orientation. The solidification process in DS is a consequence of the thermal gradient created between the upper portion of the ceramic shell mould being in a heated furnace and the chill plate, which is extracting heat from the bottom of the mould. After solidification starts, the water-cooled chill plate is lowered gradually, withdrawing the ceramic shell mould filled with molten metal from the heated furnace (Dong, 2007:3). Heat loss is now controlled by radiation from the shell mould to the cold vacuum chamber walls. A baffle can be placed at the bottom of the furnace to increase the thermal gradient. The initial DS structure begins with the starter block above the chill plate, and proceeds to fill the entire mould cavity.

The inclusion above the starter block of a helical constriction is how SC castings are obtained. The spiral grain selector facilitates dendrite branching to ensure that only one

single grain eventually survives at the top of the seed. This is because superalloys solidify by dendritic growth. The selected grain then fills the shell cavity as in the case of the DS casting.

The second method of manufacturing single crystal structure is seeding. The difference between grain selector method which control to pass through only one crystal and seed crystal method is the seed of specific orientation is placed on the chill plate in vacuum furnace. The seed was already prepared before casting process. The controlling parameter of the seed is temperature for preventing melting and allow molten metal to solidify with the same orientation as seed crystal. The benefits of seed method is that the the orientation of the metal that grows from the crystal can be controlled, to a degree, by the orientation of the crystal.
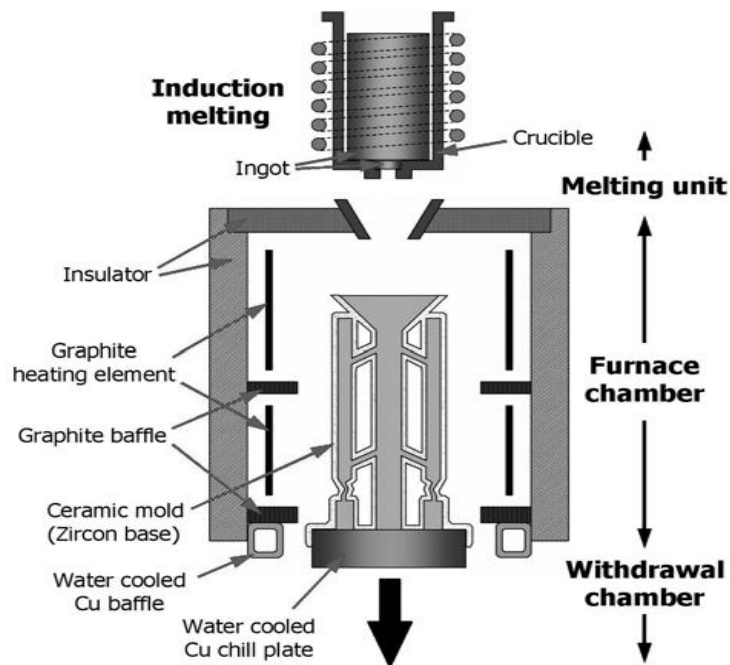
Figure 2.12: ALD machine for DS and SC casting
(Adapted from Seong-Moon Seo et al 2009:392).

CHAPTER THREE: NUMERICAL MODELLING OF VACUUM INVESTMENT CASTING

3.1   Cellular Automation Finite Element Model

Computational modelling, which has enabled extensive use of mathematical models for complex problems, has brought engineering disciplines into the realm of sciences of which the mechanics of solidification is a prime example.   Once computational techniques developed into a basic tool for solving the mechanics of solidification, it became possible to address the issues of solid/liquid (S/L) interface dynamics at the microstructural level. The modelling of dendritic growth is particularly difficult because the shape of the solid/liquid interface needs to be defined. In 1947, Ivantsov derived a mathematical solution to solve the solute transportation around the dendritic tip.   Using Ivantsov's solution, Kurz, Giovanola and Trivedi (1986) proposed a theoretical model, the KGT model, to describe the growth of columnar dendrites.

Cellular Automata (CA) solidification models aim to produce complex physical phenomena with simple rules defined at a microstructure level (Rappaz et al. 2003:460). Combined with finite element models for heat flow, Gandin and Rappaz (1997) developed a Cellular Automata Finite Element (CAFE) model to calculate the nucleation and growth of each individual grain during solidification. The envelop of evolution of the growing grains is achieved using the KGT model (Kurz et al. 1986:29) which connects growth velocity to tip undercooling. This model is used in this study to predict grain structure and orientations during solidification.

As mentioned, the CAFE model relates the grain growth rate with thermal uncooling using the KGT model, but the microscopic solute interaction is not included. Therefore, detained dendritic structure and solute segregation cannot be solved in the CAFE model.   To simulate the growth of dendrites controlled by diffusion, a model called µMatIC was developed which combines a stochastic nucleation model and a modified decentred square/octahedron method to describe dendritic growth with a finite difference computation of solute diffusion (Mirihanage et al. 2013:220). This model was first developed by Lee and co-workers (1994) to predict porosity in shape cast aluminium alloys.

At the macroscopic level, attempts have been made to study the mould filling, solidification, thermal balance of the mould and the development of stresses and strains. ProCAST has been developed based upon the finite element method (FEM) and the modelling techniques described above. It allows the modelling of heat transfer, including radiation with view factors, fluid flow and stresses fully coupled with the thermal solution (Rappaz and Dantzig, 1994).   The CAFE module, implemented in ProCAST, allows the prediction of the

morphology (shape and size) and the amount of grains in the cast. ProCAST is employed for the simulation of the directional solidification process of the casts manufactured with the Bridgman process. By applying ProCAST, it is possible to reduce the amount of experimental research by predicting the casting process parameters already at the stage of design and development.

In this research, the numerical simulation of the single crystal solidification process of turbine blades and cast rods was carried out to establish the influence of process conditions on the shape and size of columnar grains in the manufactured casts.

3.2 Modelling Grain Structure and Nucleation

There are two types of nucleation incorporated in the model: pre-fixed nucleation at specific sites and stochastic nucleation.

Pre-fixed nucleation is usually used for the simulation starting with special initial conditions, which means the nucleation at the bottom of the domain (mould surface) through seeds packed in different patterns. Certain seeds are placed into special cells with a certain level of undercooling before the simulation, and the states of these cells are turned into "growing" in advance with a small amount of fraction solid.

As opposed to pre-fixed nucleation, stochastic nucleation is incorporated to set up nuclei randomly with specific threshold undercooling, representing the stochastic nature of the process. Similar to heterogeneous nucleation, a continuous Gaussian nucleation distribution is used to relate the total number of nuclei in the bulk liquid with undercooling (Gaussian distribution). Nucleation will occur in a cell only if the cell has a randomly distributed nucleus and the undercooling in the cell exceeds the predetermined critical nucleation undercooling. Meanwhile, a random crystallographic orientation θ will be assigned to the nucleus (Dong, Lee, 2005:662).

The simulation of the grain structure growth formation of the casting was carried out using the CAFE module of ProCAST. Gaussian distribution of nucleation nuclei was adopted to account for the heterogeneous nucleation at the chill plate (Seo, 2009:393).

The grain density increase d_n, which corresponds to an undercooling increase, $d(\Delta T)$, can be described by the following Gaussian distribution:

$$\frac{dn}{d(\Delta T)} = \frac{n_{max}}{\Delta T_{\sigma} \cdot \sqrt{2\pi}} \exp\left[-\frac{1}{2}\left(\frac{\Delta T - \Delta T_N}{\Delta T \sigma}\right)^2\right] \tag{3.1}$$

where ΔT = current value of undercooling, K;

ΔT_N = mean value of Gaussian distribution, K;

ΔT_{σ} = mean value of undercooling (Gaussian distribution), K;

n_{max} = the maximum amount of substrata which enables the grain nucleation (surface nucleation, m^{-2}; bulk nucleation, m^{-3}).
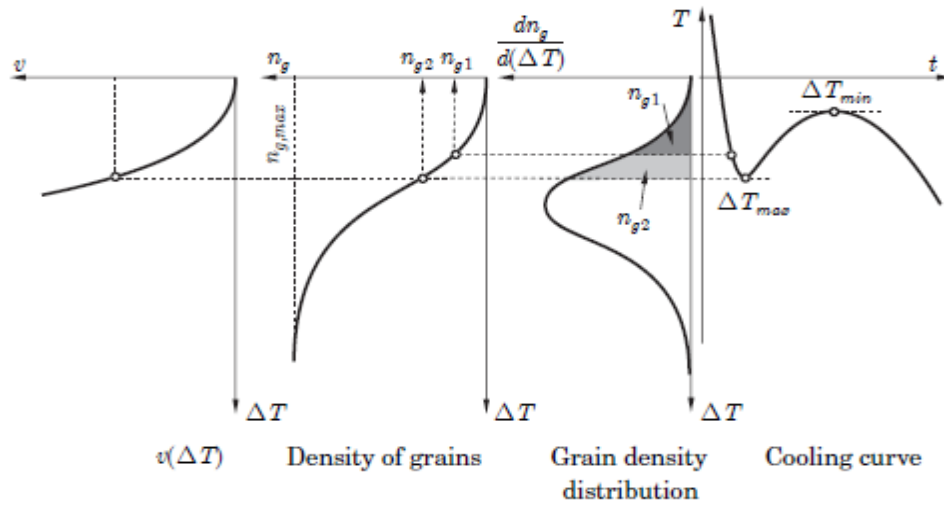
Figure 3.1: The influence of undercooling degree of liquid metal on the nuclei amount (Adapted from Dantzing and Rappaz 2009:435).

The CAFE module allows the calculation of the values of volumetric nucleation and surface nucleation parameters separately (including differentiation for selected walls). The continuous grain growth during the solidification process is caused by the undercooling of liquid metal.

The post-processing module, CAFE, was used to calculate the grain structure. In this module, the growth kinetics of the dendrite tip is calculated with the aid of the Kurz-Giovanola-Trivedi (KGT) model. In the KGT model, the undercooling of the growing dendrite tip depends on the thermal gradient, growth rate, initial composition, liquidus slope, and the partition coefficient of the solute element (Seo, 2009:394).

In the KGT model, the growth rate of the dendrite tip depends on the undercooling degree, in accordance with the equation:

$$v(\Delta T) = a_2 \cdot \Delta T^2 + a_3 \cdot \Delta T^3 \tag{3.2}$$

23

where a_2 and a_3 constants, determined by alloy composition.

The values of parameters a_2 and a_3 in equation (3.2) were established for the applied KGT model while taking into account the properties of the analysed alloy. The chemical composition of the CMSX-4 nickel superalloy and the binary phase diagrams Ni-X (X being the component of the CMSX-4 alloy) formed the basis for determining the alloying elements, depending on the temperature. The values of the distribution coefficient k and liquidus slope m were calculated for the two-component Ni-X alloy. The values of liquidus slope $\bar{m}$ and the distribution coefficient $\bar{k}$ for the multi-component CMSX-4 superalloy were determined on the basis of equations (3.3…3.5).

The total content of alloying elements is given by:

$$\bar{c} = \sum_{i=1}^{N} c_i \qquad (3.3)$$

where c_i= content of the proper element in the alloy, %wt. From the phase diagram, the liquidus slope of the alloy is given by:

$$\bar{m} = \frac{\sum_{i=1}^{N} c_i \cdot m_i}{\bar{c}}, \qquad (3.4)$$

where m_i = the slope of the liquidus line for the i-th element in the Ni-i binary system, K %wt. The distribution coefficient of the alloy is given by:

$$\bar{k} = \frac{\sum_{i=1}^{N} c_i \cdot m_i \cdot k_i}{\bar{m} \cdot \bar{c}} \qquad (3.5)$$

The calculated values of distribution coefficient and liquidus slope are presented in Table 3.1.

Table 3.1: The values of distribution coefficient and the slope of the liquidus line for the CMSX-4 nickel superalloy

Alloying element	Content of element c_i, %wt.	Distribution coefficient, k_i	Slope value m_i, $K \cdot \%wt.^{-1}$
Ni – Cr	6.5	0.65	-1.9
Ni – Co	9	1	-0.4
Ni – Mo	0.6	1	-0.001
Ni – W	6	1	-2.4
Ni – Ta	6.5	0.25	-2
Ni – Ti	1	0.5	-11.5
Ni – Al	5.6	0.6	-4
Ni – Re	3	0.2	-7.25
$\bar{c}$	38.2		
$\bar{k}$		0.534	
$\bar{m}$			-2.592

The values of the parameters a_2 and a_3 are determined analytically, taking into account the calculated values of the coefficients. Additionally, the following values of parameters characterising the solidification process, were applied: capillary length $\Gamma = 3.65 \cdot 10^{-7}$ K m, diffusion coefficient of the elements in liquid metal $D_1 = 3.6 \cdot 10^{-9}$ m^2 s^{-1}.

The velocity was determined according to the dendrite undercooling of the melt in order to determine the growth coefficients a_2 and a_3. The coefficients a_2 and a_3 were calculated using the CAFE module in ProCAST. The obtained values of grain growth coefficients were similar for both calculation methods: $a_2 = 3.149^{-7}$ ms^{-1}K^{-2} and $a_3 = 4.257^{-7}$ ms^{-1}K^{-3}.

3.3   Boundary Conditions

Modelling the cast solidification processes requires establishing the boundary conditions which reflect the actual heat transfer process. The directional solidification process is realised in vacuum. It was assumed that the heat exchange inside the furnace chamber occurs through radiation. Therefore, the first-type boundary conditions were applied (temperature value) for both the enclosure and the heaters.

Table 3.2: Boundary conditions

Heater emissivity coefficient : thermal insulation and thermal baffle (graphite)	0.8
Ceramic shell mould emissivity coefficient	0.7
Chill ring emissivity coefficient	0.7
Water cooling jacket (furnace) emissivity coefficient	0.6
Water cooling jacket (furnace) temperature	293 K (20 ^{0}C)

Table 3.3: Heat transfer coefficients (HTC)

Water cooled chill plate	2500 W/m^{2}K
Shell mould and casting / casting and the chill plate insulation	20 W/m^{2}K
Thermal insulation in furnace	200 W/m^{2}K
Protection tube in casting rod	300 W/m^{2}K

The heat transfer from the inner surface of the chill plate and the water chill ring is described by the boundary conditions of the third-type. The values of heat transfer coefficient h=2500 W/m^{2}K and water temperature of 293 K (20°C) were used, due to the intensive water-cooling of those surfaces.

The contact thermal resistance between the materials is of large significance for the heat transfer rate between them. This phenomenon is described by the characteristic boundary conditions of the fourth-type. Within the framework of the developed model, the authors established those boundary conditions on the contact surface of the ceramic shell mould and cast as well as the cast and the chill plate (h =20 W/m^{2}K). The same boundary conditions were also used for the thermal insulation boundary inside the furnace (h=200 W/m^{2}K). A constant value of heat transfer coefficient (h=300 W/m^{2}K) was assumed on the contact surface of the protection tube, the ceramic shell mould and the cast.

3.4   Material Constants used in Numerical Simulation

The materials used for simulation were selected in the ProCAST module. The thermal and physical properties, including the material of ceramic shell mould, were chosen for particular materials of the system. The thermal and physical properties, characterising the CMSX-4 nickel superalloy, were chosen for the models of turbine blades and cast rods and the gating system.

3.5   Numerical Simulation

The values of distribution coefficient $\overline{k}$ and slope of liquidus curve $\overline{m}$ determined for the CMSX-4 alloy were applied in order to calculate (according to the KGT model) the growth rate of the dendrite tip, depending on the degree of liquid alloy undercooling. The numerical simulation and the temperature measurement in the ceramic shell mould were conducted in order to determine the duration of the mould annealing process, before pouring the liquid metal The ceramic shell mould was placed on the chill plate in the furnace heating chamber and was annealed to the temperature of 1793 K (1520°C). During the initial stage of the heating process, the heating rate reaches its highest value. The heating rate of the mould decreases afterwards and, after a certain amount of time, becomes constant. The further annealing of the mould causes a slight increase in its

temperature. The analysis of the results obtained led to the conclusion that the duration of the annealing process of the ceramic shell mould is long and there is a possibility of reducing it.

Computer aided design (CAD) geometry of the investment casting process and ceramic shell mould were used to generate a mesh representing each of the prospective materials during the solidification process. For comparison, the mesh of the mould of ceramic shell and casting (two blades and one casting rod) is shown in Figure 3.2.
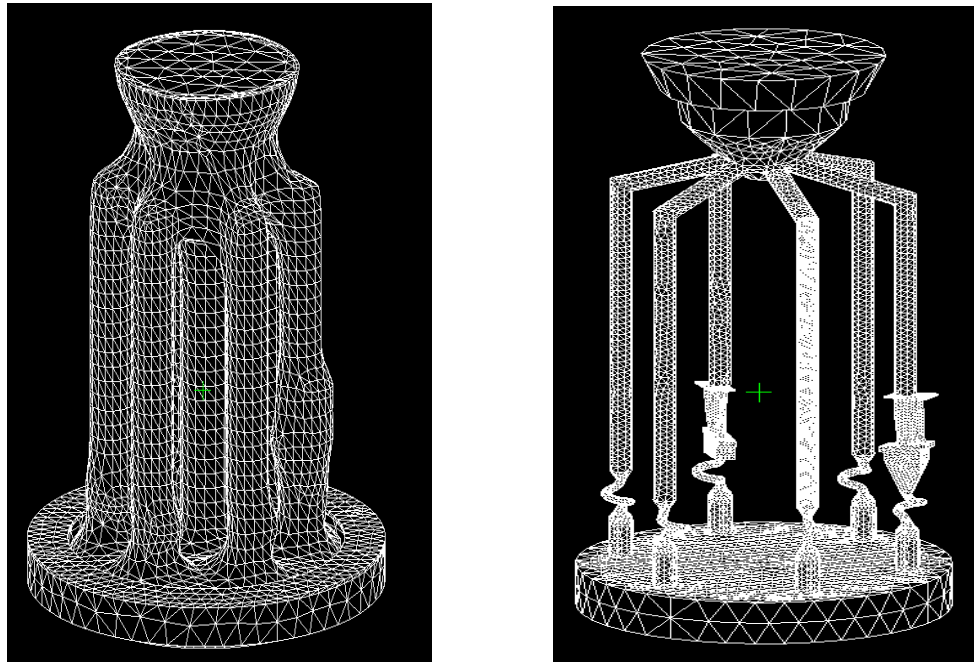
Figure 3.2: Results of meshing for ceramic shell and casting.

The temperature distribution along the mould height is non-uniform. The influence of the chill plate causes under-heating of the ceramic shell mould, at the distance of approximately 25 mm from the plate. It is noted that the correct value of the heat exchange coefficient between the ceramic shell mould and the chill plate is significant.
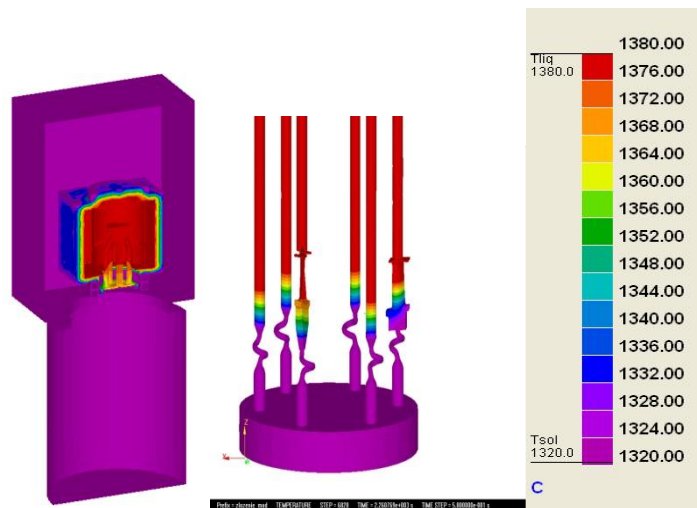
Figure 3.3: The predicted temperature distribution in the furnace heating chamber, the casting mould and the cast

During the modelling simulation process, its inflated value results in underheating of the ceramic shell mould. It also causes the cooling rate of the low part of both the mould and the cast to attain high values. Small-sized equiaxial grains and nuclei form on the surface of the chill plate. The zone of frozen crystals is created, containing dendritic branches which are characterised by different crystalline orientation, in relation to the heat flux direction.

The solidification of the liquid metal starts with the cold copper chill plate, where equiaxed grains nucleate. These grains grow and then enter the grain selector. During this stage, a grain selection mechanism, based upon the best alignment of the [001] crystallographic orientation with the heat flow direction, operates. Therefore, only one single grain ideally passes the selector. Its crystallographic [001] orientation should be within 15^0 of the blade's length axis in order to achieve the desired mechanical properties.

When the dendritic solidification front passes a re-entrant corner, such as the root of the blade, the secondary arms of the dendrites neighbouring the mould wall can grow into the open liquid space. They are usually facing the liquid, which is more undercooled, and can therefore grow faster than the primary arms. However, if the undercooling of the liquid close to the mould wall is large enough, heterogeneous nucleation sites may be activated before the secondary arms reach the surface of the mould, forming stray grains.

Shifting the ceramic shell mould to the cooled space of the furnace and the directional heat abstraction results in undercooling of the next volume of liquid alloy. The dendrite branches, which are oriented parallel to the direction of heat flux, have the largest probability of sustaining their further growth. Therefore, only certain dendrites branches,

28

oriented in a privileged direction, continue to grow. The dendrites with unprivileged growth directions decay in the cast rod. Columnar-shaped crystals are formed - their growth direction being parallel to the direction of heat flow. The microscopic examination revealed that the area of the most intensive alloy undercooling at the beginning of the cast rod (contact of the chill plate with the cast) is characterised by the largest amount of grains. The amount of grains decreases with a rise in the distance of the solidification front from the chill plate.

CHAPTER FOUR: VACUUM INVESTMENT CASTING TECHNOLOGY

4.1 Development of the Vacuum Investment Casting Process

In the sixteenth century the process of investment casting was commonly called lost-wax casting. It was found that investment casting was very effective in creating shapes for hot-stage parts. Before 1940, turbine engine blades were produced from iron alloys through cold wrought. In the 1940s and 1950s, investment casting using vacuum melting furnace was introduced to manufacture engine blades to remove undesirable alloy impurities. In 1970, the directional solidified crystal structure process was invented to improve the thermal capability of the blades. The mechanical properties were significantly improved in that crystal growth was aligned in the direction of centrifugal forces (grain boundaries decreased). Using such directional solidified techniques lead to the creation of single crystal blades (Chilton, 2002:25). The modern process of manufacturing turbine blades is shown in Figure 4.1.

Wax Injection	Wax Assembly	Ceramic dipping
Ceramic coating	Drying ceramic shell	Dewaxing
Pouring metal	Ceramic shell removal	Cast removal
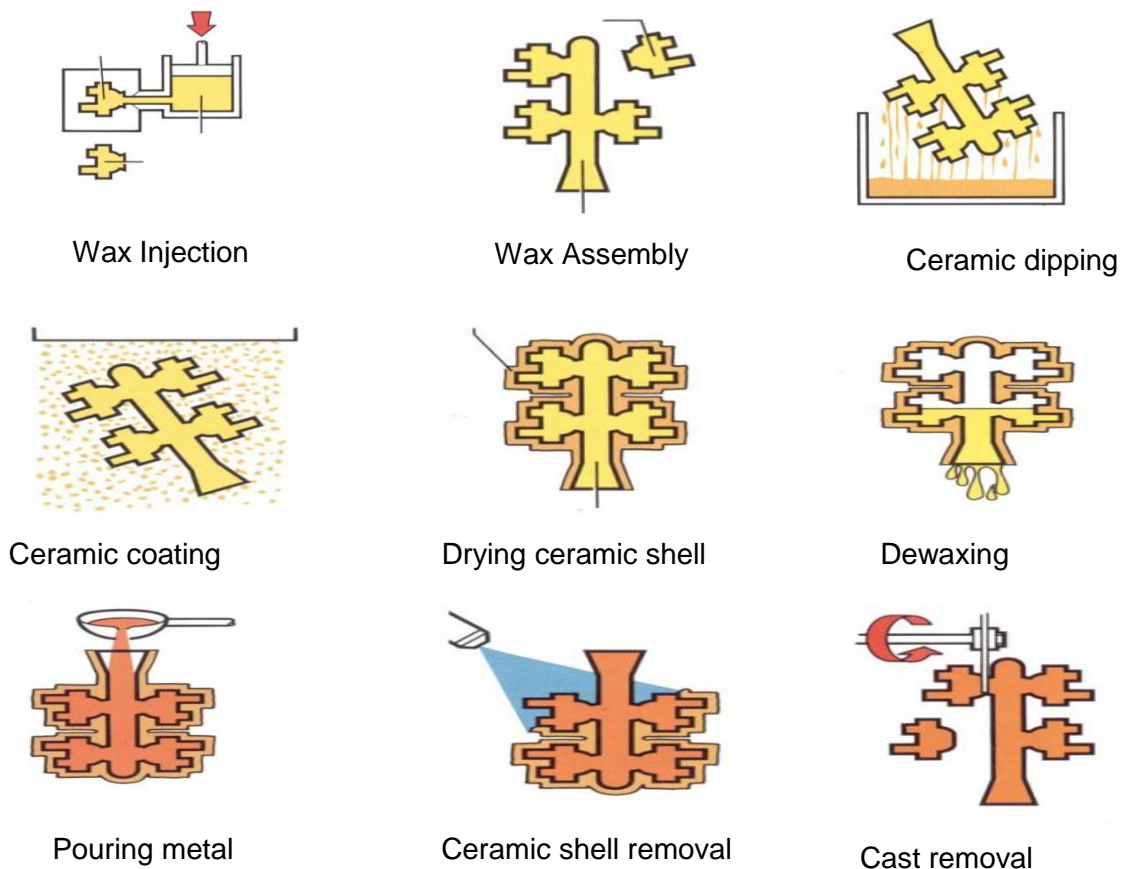
Figure 4.1: Schematic illustration of the investment casting process.

The investment casting process include the following steps:

1. A pattern is prepared by injecting molten wax into a metal mould. Wax patterns can be assembled in clusters to enable several blades to be produced in a single casting.
2. The wax mould is then dipped into a ceramic slurry consisting of binding agents and mixtures:
    - prime coating alumina (Al_2O_3) and silica (SiO_2) 30 % suspension in H_2O;
    - second coating mullute–alluminum silicate [$Al_6O_5(SiO_4)_2$] and silica (SiO_2) 30 % suspension in H_2O.

    This process needs to be repeated several times until the shell thickness is thick enough to withstand the mechanical shock of receiving the molten metal.
3. After the shell mould is constructed, the wax is removed in an autoclave and, for flash de-waxing, the ceramic moulds are placed in a furnace and preheated to a high temperature to build up its strength and make it ready to receive the molten superalloy.
4. The ceramic mould is checked for any cracks and holes with colouring water as well as the measuring volume of molten metal.
5. Pouring molten metal into the ceramic shell and cooling down until the metal has solidified.
6. When the casting is finished, the investment shells are knocked off, and the casting is then sand blasted.
7. Cut the casts and runner bars.

The above steps are illustrated in Figure 4.2 below.
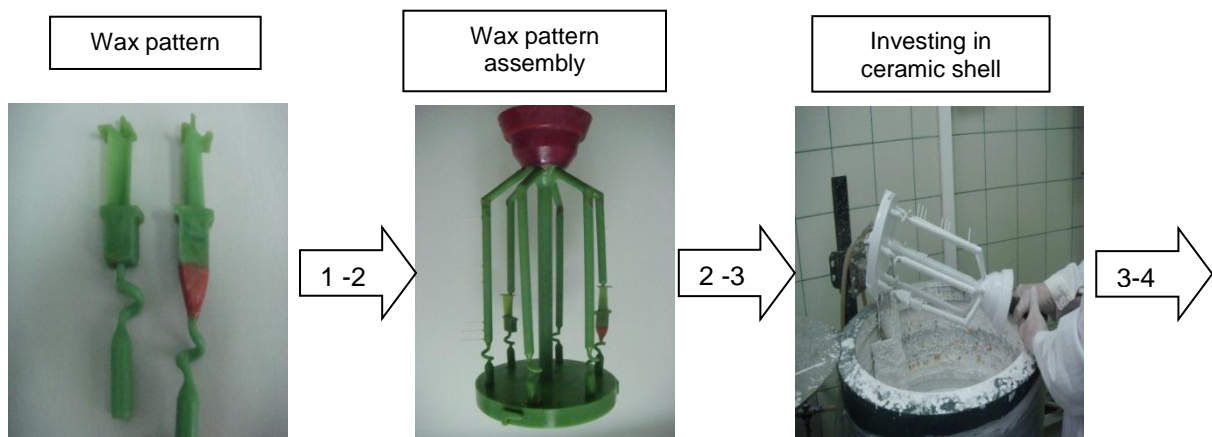
Figure 4.2 : Pictorial illustration of the vacuum investment casting process for DS and SC castings *(continued on next page).*
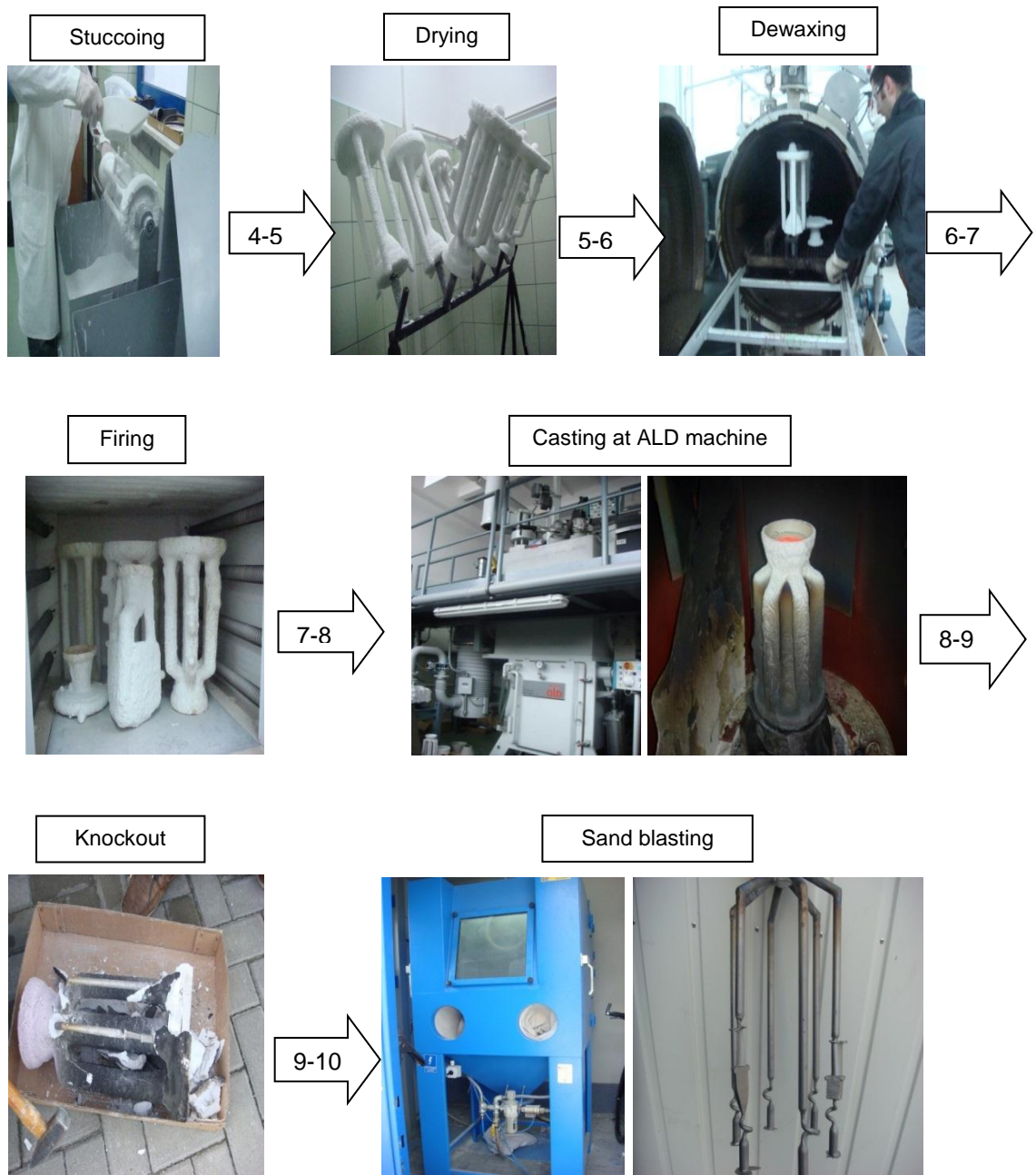
Figure 4.2: Pictorial illustration of the vacuum investment casting process
for DS and SC castings.

4.2 The Bridgman Process for Vacuum Investment Casting

The directionally solidified single crystal process for turbine blades made of CMSX-4 nickel superalloy was performed using the Bridgman method, in a VIMIC 2 E – DS/SC vacuum furnace manufactured by ALD Vacuum Technologies. The furnace belongs to the Research and Development Laboratory for Aerospace Materials at Rzeszow University of Technology.

The heating chamber consists of two heaters with 300 mm diameter and thermal insulation. The chill rings, with a diameter of 250 mm, were placed under the heating chamber. Additionally, the presence of the graphite thermal baffle with a diameter of 220 mm and a thickness of 2.5 mm was taken into consideration in the development of the model. Introduction of the baffle is meant to decrease the heat losses and rise of temperature gradient in the cast. The finite element mesh used during calculations also includes the internal surface of the melting chamber and the cooling chamber of the furnace.

Based on directional solidification (DS or SC), the molten alloy is poured into a hot ceramic mould at a temperature of approximately 1520°C, which is maintained by radiant heating in the furnace. A water-cooled copper chill plate is located at the bottom to make the solidification start at the bottom. During solidification, the solid-liquid growth front can be controlled by heat flow in the mould. By slowly withdrawing the mould out of the furnace, metal solidifies directionally from bottom to top, producing large, columnar grains or a single crystal elongated in the direction of withdrawal, markedly improving the creep properties. In single crystal (SC) castings, to entirely remove the transverse grain boundaries, a grain selector is added at the base of the mould. As a result, only one grain with a preferred orientation can eventually survive at the top of the grain selector and grow into the main body of the turbine blade, which allows the structure to be free of high angle boundaries (HABs). Since HABs in superalloys are preferential sites for crack initiation, the creep resistance of SC structures is dramatically improved. Depending on the size of the blade, the entire process takes 3-6 hours to complete.

4.3   Experimental research

The 3.5 kg material was inductively melted. Its solidification process was conducted in vacuum to avoid oxidation of reactive elements in their composition. The ceramic shell mould was placed on the chill plate and annealed in the heated space of the furnace, at a temperature of 1793 K (1520°C) for 0.5 hour. The moulds were poured with the CMSX-4 nickel superalloy (Table 3.1) at the temperature of 1793K (1520°C), for approximately 3 seconds.

After pouring with liquid metal, the ceramic moulds were shifted from the heated space to the cooled space of the furnace with different velocities for each of the experimental castings as follows:

- First experiment withdrawal velocity: v_w = 1 mm/min;
- Second experiment withdrawal velocity: v_w = 3 mm/min;
- Third experiment withdrawal velocity: v_w = 5 mm/min.

For the experimental analysis, three wax pattern models were deployed, each having two turbine blades with different configurations of blade and grain selector with starter block (turbine blade 1 and turbine blade 2, Figure 4.3). Additional wax models of one casting rod (diameter 12 mm) with thermocouples and three casting rods without thermocouples were deployed for mechanical and microstructural investigations.
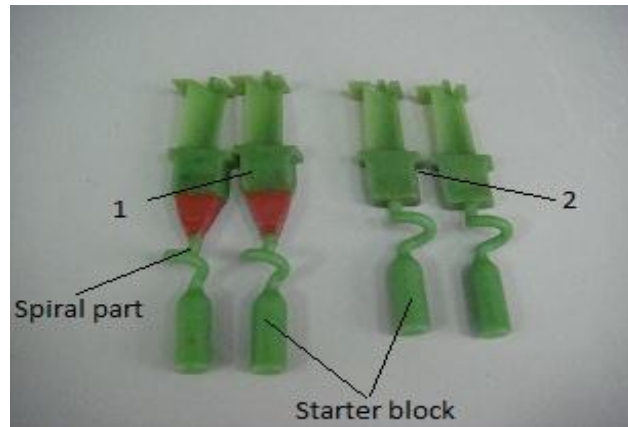
Figure 4.3: Turbine blades (1, 2) with different geometry

The temperature measurements of the castings were recorded during the solidification process as well as the further cooling process. The results obtained were used as a base for verification of the imposed boundary conditions, calculated nucleation coefficients and grain growth rates in the castings.

The methodology for cast temperature measurement was developed. In this method, type B thermocouples (PtRh30, PtRh6) with a diameter of 0.2 mm were used. The thermal insulation system and heaters made of graphite are a source of carbon in the heating chamber of the furnace. Carburisation of the PtRh wires may be a reason for thermocouple degradation. For this reason, the thermocouples were placed inside continuous ceramic insulation shields to prevent carburisation.

The temperature was measured at six points in the cast rod:

- for velocity 1 mm/min at the height of: 66, 78, 145,156,167 and 234 mm (see Figure 4.4);
- for velocity 3 mm/min at the height of: 69, 81, 142, 159, 170 and 236 mm;
- for velocity 5 mm/min at the height of: 66.5, 79, 145, 157, 168 and 234 mm.
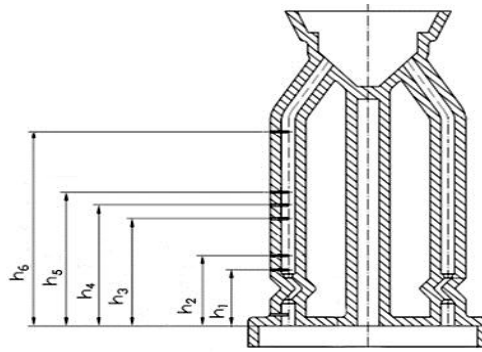
Figure 4.4: Ceramic shell with thermocouple points.

An automatic data acquisition and control system was implemented to collect the data and record the curves of temperatures of change with time at these positions. The junctions of thermocouples were secured against the influence of liquid alloy by placing them inside the one-hole shields with an outer diameter of 2.5 mm (Figure 4.4). The thermocouple wires, which were outside the mould, were placed inside two-hole ceramic shields with an inner diameter of 0.6 and outer diameter of 3.5 mm. The homogeneous ceramic shields were developed and applied in order to protect the thermocouple wires against carbon degradation.

The prepared wax patterns were used for manufacturing the multilayer ceramic shell moulds. After application of ten layers, the average thickness of the ceramic shell mould wall was approximately 10 mm. Figures 4.5 - 4.7 shown steps of process manufacturing turbine blades.

Figure 4.5: Thermocouples in wax pattern bar to identify temperature distribution at different withdrawal rates of solidification process.

Figure 4.6: a) Wax pattern of turbine blade and castings rods; b) ceramic shell mould with thermocouples connected to ALD machine.

Figure 4.7: The casting assembly after removal of the ceramic shell and sandblasting.

4.4 Experimental results

The temperature measurement results obtained from the thermocouples are presented below (see Figure 4.8…4.10), from which the temperature gradients can be established in 4.5. An automatic data and control system was implemented to collect the date from ALD machine and record the curves of temperature change with time at these positions.
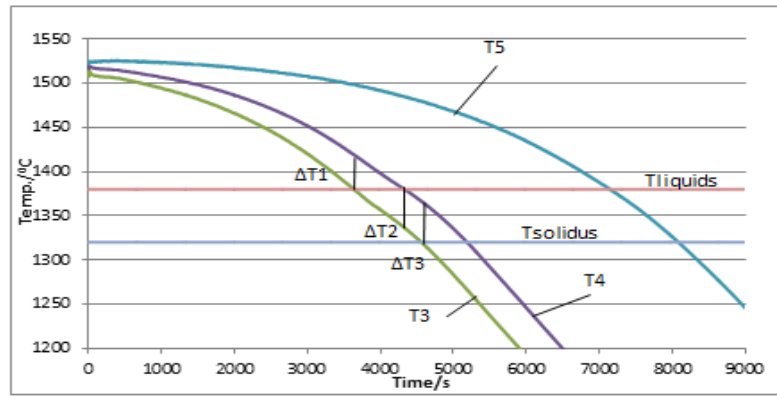
Figure 4.8: Experimental thermal curves at different heights in casting rod for velocity 1 mm/min (thermocouples T3, T4 and T5).
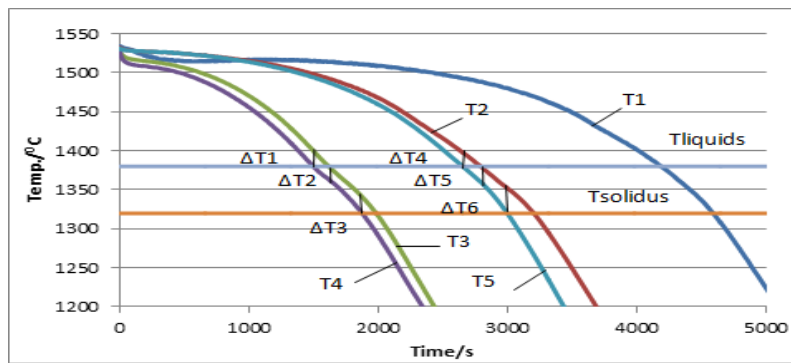
Figure 4.9: Experimental thermal curves at different heights in casting rod for velocity 3 mm/min (thermocouples T1…T5).
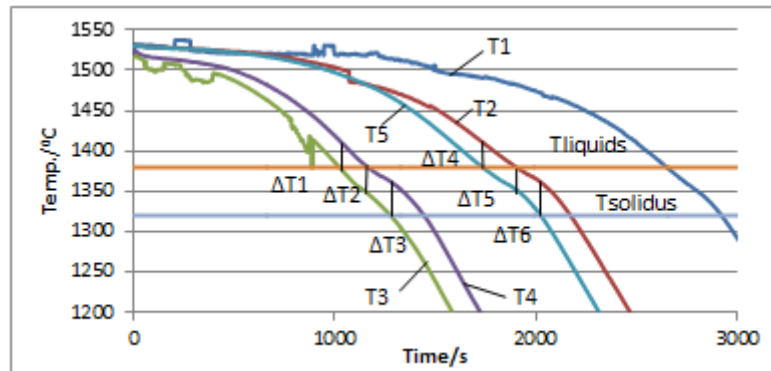
Figure 4.10: Experimental thermal curves at different heights in casting rod for velocity 5 mm/min (thermocouples T1…T5).

The temperature measurements for casting experiments established at selected points of the casting road were a basis for determining the average temperature gradient in the mushy zone at three areas (ΔT_1…ΔT_6).

The entire heating cycle for the SC process is shown in Figure 4.12 below for turbine blade withdrawal velocity of 5 mm/min. It consists of the following steps:

1. Heating furnace 1500 ^{0}C - 45 min;

2. Annealing CMSX-4 - 30 min;

3. Pouring melting metal CMSX-4 into the ceramic shell – 5 s;

After pouring liquid metal into the ceramic shell mould, the liquid alloy temperature decreases until the solidification temperature / liquidus point is reached. The temperature drops below the liquidus point and, upon obtaining the required undercooling, leads to nucleation of γ phase grains in the liquid alloy.

4. Cooling down - moving the ceramic shell with molten metal to the cooling chamber – duration 60 min.

The simulation results observed indicated that the nucleation temperature of γ phase depends on the cooling rate of the liquid metal.
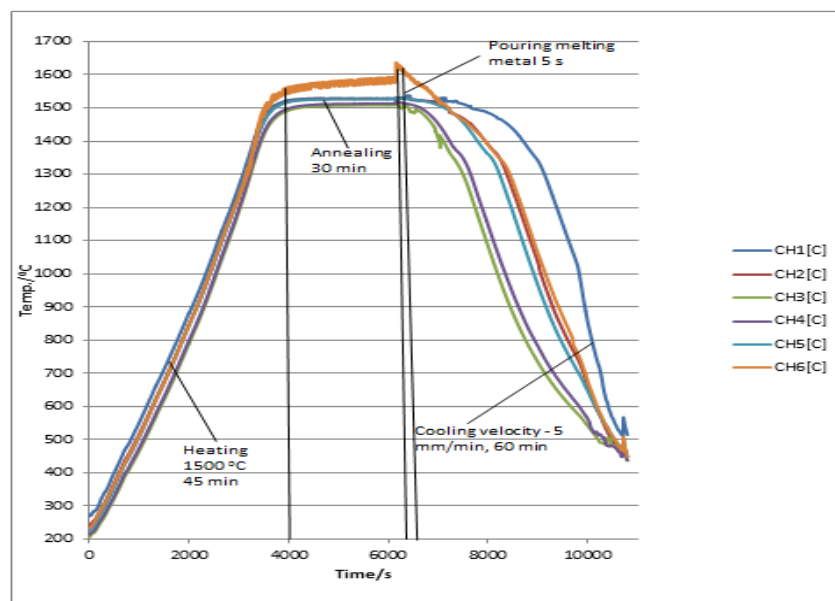
Figure 4.11: Heating cycle diagram for velocity 5 mm/min (CH1 … CH6 thermocouples connected to ALD machine).

The results of the numerical simulation of the temperature distribution were analysed and used as a basis for establishing the characterisation of the casting of the turbine blade during the solidification process.

Figure 4.12 below compares thermocouple 1 for withdrawal velocities of 3 and 5 mm/min.
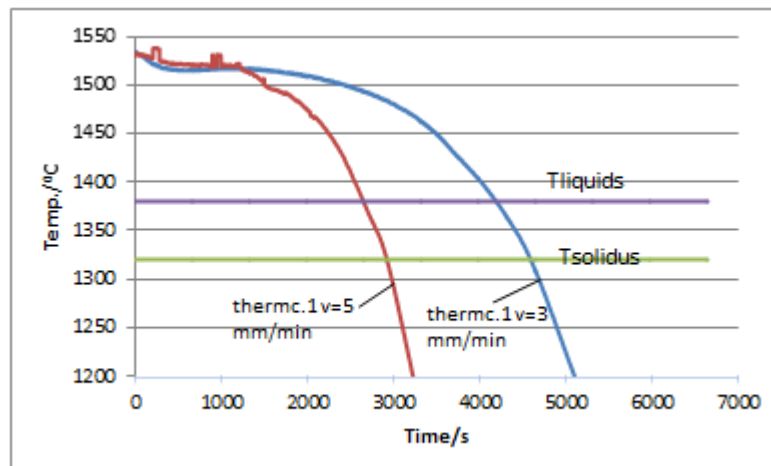
Figure 4.12: Thermocouple 1 curves for withdrawal velocities 3 and 5 mm/min.

Figure 4.13 below compares thermocouples 3, 4 for withdrawal velocities 1, 3 and 5 mm/min.
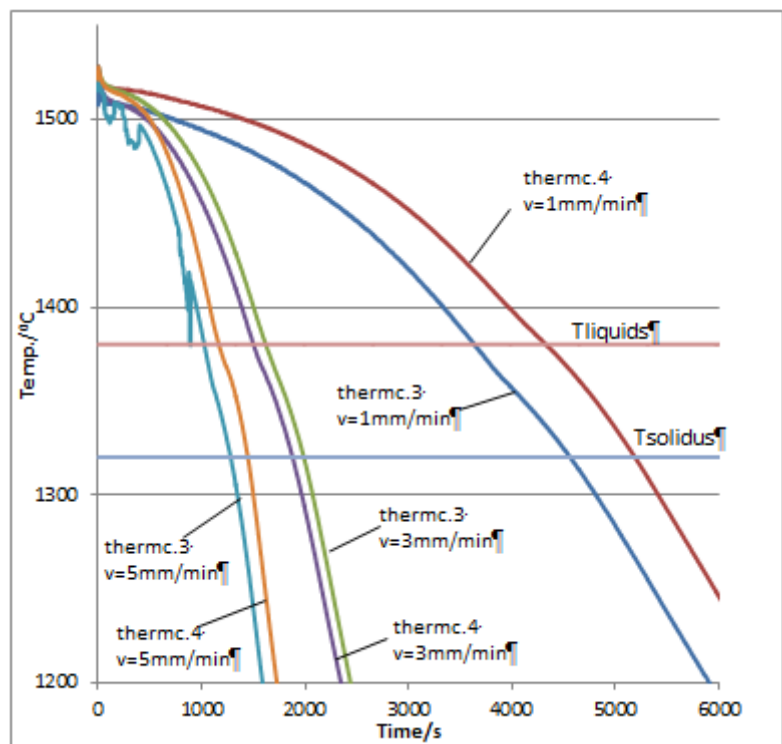
Figure 4.13: Thermocouples curves 3, 4 at different velocities (1 mm/min, 3 mm/min and 5 mm/min).

The effect of withdrawal velocity on the microstructure will be examined in Chapter 5. For now, it is observed that the withdrawal velocity plays a role in determining the mechanical and chemical properties (i.e. microstructure) of the final product, in this case, that of the turbine blade castings.

4.5 The analytical calculation of the temperature gradient

Using the temperature-time graphs allows the calculation of the temperature gradients at different heights in the casting rod. Calculations were carried out using Figures 4.8…4.10 for each of the experiments, using the equation for temperature gradient. It was calculated by dividing the difference (ΔT_1) between the temperature in the test point (L_{i+1}) and the solidus temperature in the point (L_i).

$$G = \frac{\Delta T}{L} = \frac{T_{i+1}(t) - T_i(t)}{L_{i+1} - L_i}$$ (4.1)

where G = Temperature gradient, ^{0}C/mm;

$\quad\quad T$ = Temperature, ^{0}C;

$\quad\quad L$ = Length, mm.

The calculations are shown in the tables below 4.1… 4.3.

Table 4.1: Values of temperature gradient in the mushy zone (at different heights) for withdrawal velocity 3 mm/min.

	The temperature gradients in mushy zone for thermocouples 4,3			The temperature gradients in mushy zone for thermocouples 5,2		
The distance of the test point to cast base, mm.	h_4 =81	h_3 =69	-	h_5 =142	h_2 =159	-
The temperature difference between points $\Delta T, {}^0C$.	20.5	16.5	21.0	18.0	19.5	32.5
Distance between the test points, mm	12	12	12	17	17	17
Temperature gradient, ^{0}C/mm.	1.7	1.4	2.0	1.1	1.2	1.9

Table 4.2: Values of temperature gradient in the mushy zone for withdrawal velocity 1 mm/min.

	The temperature gradients in mushy zone for thermocouples 4,3		
The distance of the test point to cast base, mm.	h_4 =78	h_3 =66	-
The temperature difference between points $\Delta T, {}^0C$.	39.5	43	46.5
Distance between the test points, mm.	12	12	12
Temperature gradient, ^{0}C/mm.	3.3	3.6	3.9

Table 4.3: Values of temperature gradient in the mushy zone for withdrawal velocity 5 mm/min.

	The temperature gradients in mushy zone for thermocouples 4,3			The temperature gradients in mushy zone for thermocouples 5,2		
The distance of the test point to cast base, *mm.*	h_4 =79	h_3=66.5	-	h_5 =145	h_2 =157	-
The temperature difference between points $\Delta T, {}^0C$.	20.5	16.5	21.0	18.0	19.5	32.5
Distance between the test points, *mm.*	12	12	12	17	17	17
Temperature gradient, ^{0}C/mm	2.8	2.7	3.5	1.8	1.6	2.4

The temperature gradient varies along the cast height. The height of mushy zone of the casting rod depends on the position of ceramic shell mould. This height is dependent on the temperature gradient and the cast cooling rate.

As the withdrawal velocity is increased, the solidification rate increases and duration of the cast solidification process decreases along the casting rod height, above the transition region between the grain selector and the casting rod. High thermal gradients during single crystal solidification, however, can achieve finer dendrite arm spacing, reduced grain defects, and reduced element segregation. The thermal gradient ahead of the liquid/solid interface (GL) is a key parameter that assures sequential solidification along the axial direction and prevents equiaxed grains from occurring under constitutional undercooling in the melt.

However, this does not necessarily guarantee the SC structure for the higher withdrawal velocities due to related casting defects that may arise.

CHAPTER FIVE: MODELLING FORMATION OF SINGLE CRYSTAL NI SUPERALLOY

5.1   Diffraction Analysis for Single Crystal structures

5.1.1 Introduction

The Laboratory in Rzeszow university of Technology has a specialised X-ray diffractometer to determine the crystal orientation distribution on the surface of a single crystal structure - including single crystals of large sizes - such as the blades of 1st and 2nd stage in high pressure turbine aircraft engine. The diffractometer is equipped with a goniometer allowing research on three-dimensional surfaces. The strength of metals decreases with increasing temperature. Since mobility of atoms increases rapidly with temperature, it can be appreciated that diffusion–controlled processes can have a very significant effect on high-temperature mechanical properties. The assessment of crystalline quality, including the crystallographic orientation, is a very important element of manufacture of single crystal blades casts made of nickel superalloys.

Superalloy properties change depending on the crystallographic direction. Hence, the assessment of single crystal casts through the determination of their crystallographic orientation is the basis to determine mechanical properties. In line with this, it has been determined that an increase in the angle between direction [001] and the direction of growth results in decreased mono-crystal creep resistance. Based on such results, it has been assumed that the value of the angle of direction [001] deviation from the direction of single crystal growth axis should not exceed 15° for acceptable mechanical behavior of single crystal structures.

An X-ray EFG diffractometer can be used for the assessment of the structural quality of multi-component single crystal nickel superalloys, through determining the crystal orientation of single crystal elements of large size. Together with specialised software, the main axis [001] and perpendicular axis [100] of the crystal can be determined as well as the tilt angle value of the axis [001] of crystal growth, effectively by a non-destructive method.

The EFG diffractometer is equipped with a copper tube and two detectors Figure 5.1. A 3D image of the studied object is obtained by laser beam scanning. Then a map (distribution) of crystallographic orientation on the studied surface of the single crystal is created. The determination of crystallographic orientation on a 3D surface is especially significant due to technological reasons – it creates a non-destructive method for the crystallographic orientation studies of single crystal blades of aircraft engine turbines Figures 5.1, 5.2 (Onyszko, 2010:2).

<center>(a)   (b)</center>
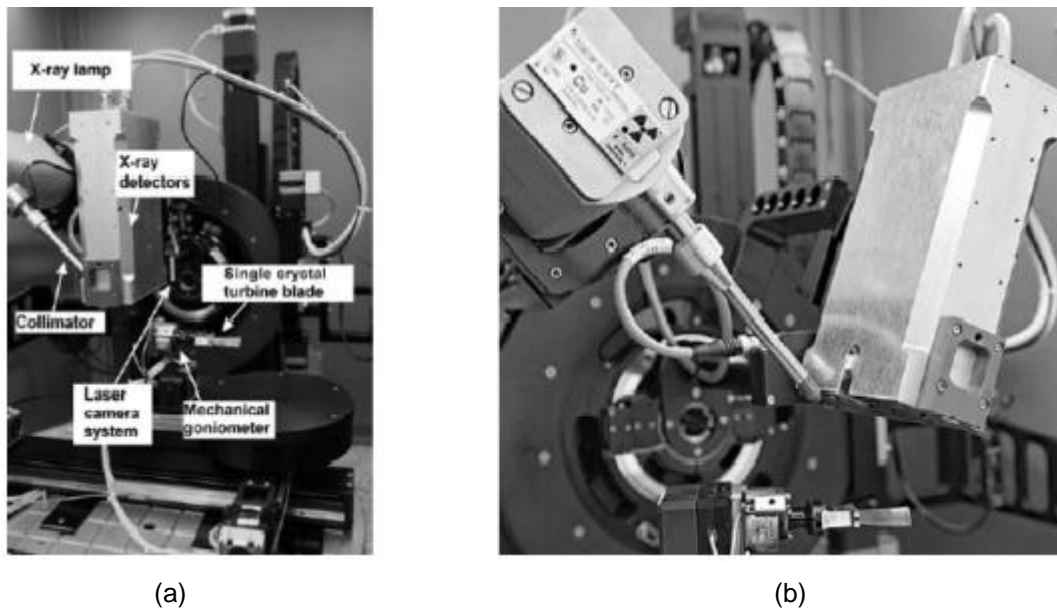
Figure 5.1: EFG diffractometer for full crystallographic orientation of single crystal blades made of nickel superalloys: a) general view, b) goniometer for single crystal blades (adapted from Onyszko 2012:2).
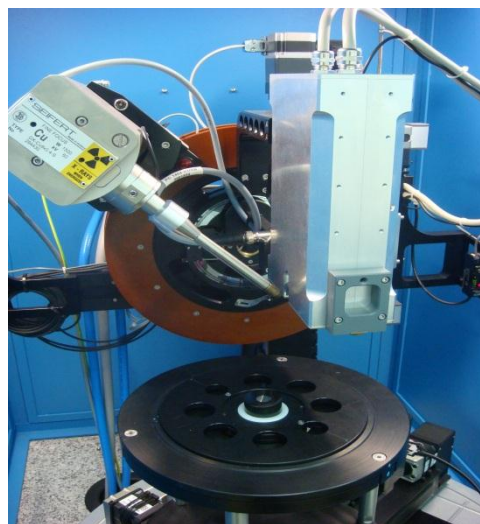
<center>**Figure 5.2:** OD-EFG diffractometer with sample for crystal orientation.</center>

5.1.2 Experimental work

The Laue diffraction was obtained from mechanically polished, chemically etched surfaces of cross-sections of samples. Three cross-sections of SC casting rods were examined – see Figures 5.3 and 5.4 – to determine the α orientation in a single crystal structure for withdrawal velocity of 3 mm/min.

The crystal orientation research work focused on the analysis of the parameters of the real structure of turbine blades, which have significant impact on the mechanical properties of blades operating in the hot section of aircraft engines. The orientation of single crystals was

<center>43</center>

determined from the measurement of angle α. Angle α has been defined as the deviation of the [001] γ' direction from the blade axis Z of growth (Onyszko, 2010:3).
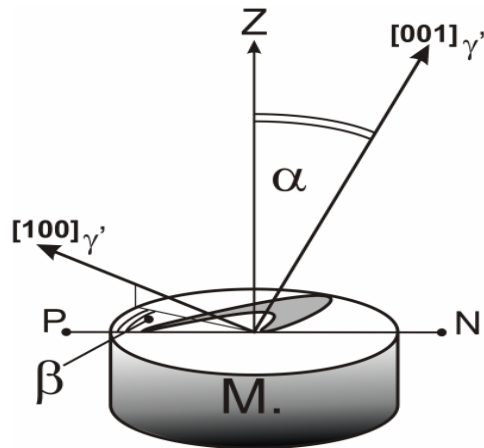
Figure 5.3: Schematic illustration of α angle on spaceman
(adapted from Onyszko 2010:1327).

Figure 5.4: Cross sections of casting road 3 mm/min.

5.1.3 Results for cast samples

At the withdrawal rate of 3 mm/min, the cross-sections of the rods were obtained, in which changes in the angle α along the blade axis have the smallest range (see Figure 5.5, Table 5.1). This proves a high degree of structural homogeneity.

(a)   (b)   (c)
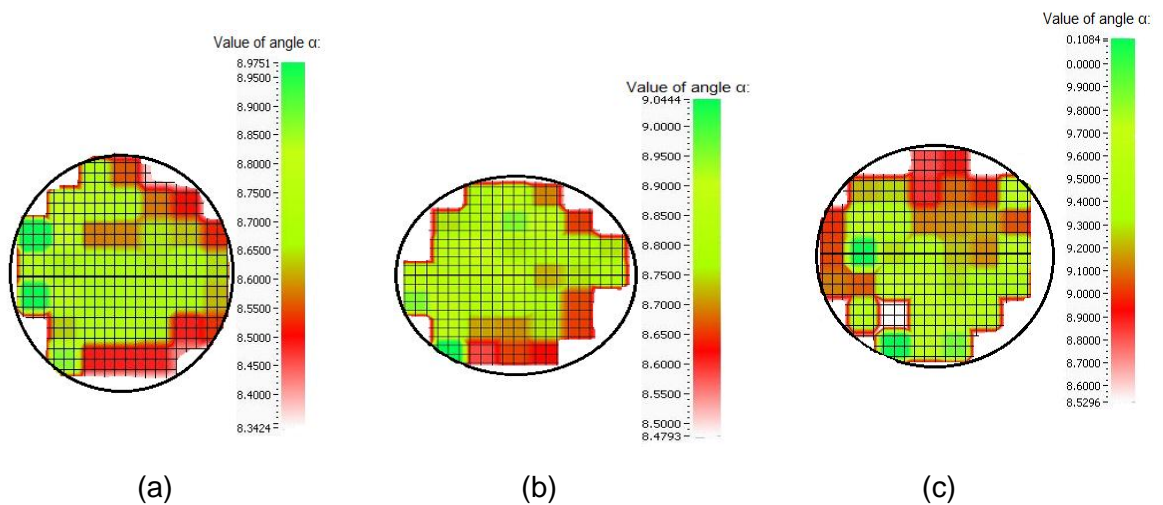
Figure 5.5: Deviation angle α at the base, in the middle and at the top of the rod casted with withdrawal rate 3 mm/min.

The map (distribution) of the crystallographic orientation on the studied surfaces for withdrawal velocity 3 mm/min is given in Table 5.1, showing deviation angle α between 8.75 and 9.40.

Table 5.1: Values of angle α describing the deviation of the [001] γ' direction from the single-crystal bar axis.

Spacimen	Withdrawal rate (mm/min)	α ± 1⁰
1	3	8.75
2	3	8.8
3	3	9.4

The other cross-sections for samples with withdrawal rates of 1mm/min and 5 mm/min were also investigated. These experiments did not show values of angle α. It was assumed that the withdrawal velocity was either too slow (1 mm/min) or too fast (5 mm/min) for good crystal growth orientation - to confirm the assumption that the observed disorientation angles on cross-sections for withdrawal rates of 1mm/min and 5 mm/min related to the width of the interdendritic areas.

5.1.4 Results for heat treated samples

To compare the effect of heat treatment on crystallographic orientation, diffraction analysis for samples of withdrawal velocity 3 mm/min after heat treatment was carried out. The parameters of the heat treatment experiments can be found in Section 5.2.
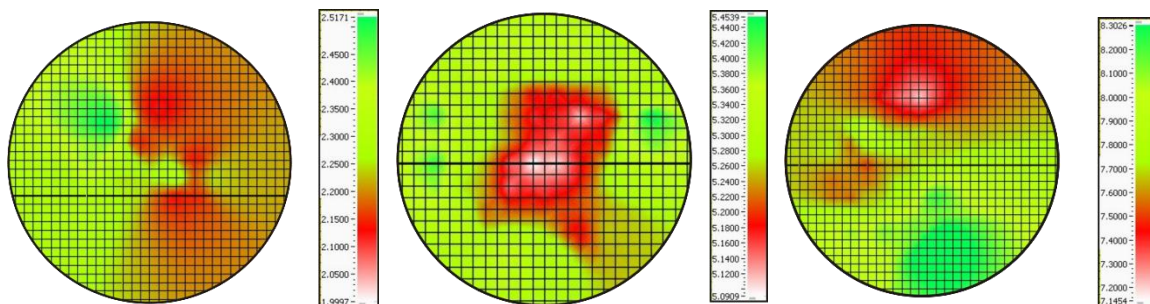
Figure 5.6: The maps of crystallographic orientation prepared using EFG diffractometer for derivation of angle α of the heat treated samples with withdrawal rate 3 mm/min.

The map (distribution) of the crystallographic orientation on the studied surfaces for withdrawal velocity 3 mm/min, after heat treatment, is given in Table 5.2.

Table 5.2: Values of angle α describing the deviation of the [001] γ' direction from the single-crystal bar axis for the heat treated samples.

Spacimen	Withdrawal rate (mm/min)	α ± 1⁰
1	3	2.20
2	3	5.09
3	3	7.70

The aforementioned experimental results, obtained with the use X-ray (EFG) diffractometery, allows the comparison of crystallographic orientation in as-cast and heat treated samples. This work is important as the quality of single crystal turbine blade and mechanical properties depend on crystallographic orientation.

All values of the angle α are smaller than 15^0 and comply with global manufacturing standards in the aircraft industry. The lowest value of the angle α are found for the samples after heat treatment. This allows the conclusion that heat-treated blades have the highest creep resistant properties.

5.2 Heat Treatment Research

The all-important mechanical properties for turbine blades depend largely on the alloy composition, but also rely on proper heat treatment. Traditionally, two heat treatment techniques are used for nickel-based superalloys. The first is the solution heat treatment technique, designed to homogenise the microstructure and reduce the effects of elemental segregation. The second technique involves two aging heat treatments, designed to develop a cuboidal γ and γ' microstructure.

Solution heat treatment is a very long process. Moreover, it can be quite expensive.
It takes long hours during annealing operation to slowly diffusing heavy elements (tungsten, molybdenum) and when the solidification is coarse, with primary dendrite arm spacing. The temperature must be therefore must be high enough to take into solution even the coarse interdendritic particles, but sufficiently low to avoid incipient melting samples.

The solution heat treatment is essential in order to obtain a uniform and isotropic material.

Solution heat treatment is the latest technology developed for single crystal structures and is designed to completely solution the γ' and most of the γ and γ' eutectic without incipient melting. Stress-relief treatment is also used to reduce residual stresses in the casting.

During solidification through the mushy zone, some of the solute elements prefer to remain in the liquid phase while some elements preferentially diffuse to the solid phase forming a

chemical heterogeneity in the solidified structure with a significant fraction of γ and γ' eutectic at the interdendritic region. It has been established that Co, Cr, W, Mo, and Re segregate preferentially to the dendrite cores, while Ti, Al, and Ta segregate preferentially to the interdendritic region. There are two important effects of this microsegregation in the solidified structure: chemical heterogeneity and microstructural heterogeneity. These effects have a direct impact on the mechanical properties and hence the performance of superalloys as high temperature materials (Hedge et al, 2010:5530).

The γ' precipitates in the interdendritic region of a solidified structure are coarse, irregular shaped and incoherent. Since the γ and γ' interface plays a major role in the development of strength and creep resistance, it is always desirable to have fine, uniform and coherent cuboidal shaped precipitates throughout the microstructure. The chemical heterogeneity in the solidified structure leads to chemical instabilities. Dendrite cores in the solidified structure being rich in Cr and Re are preferred locations for formation of the embrittling TCP (topological close packed) phases that degrade both the creep and fatigue resistance of the alloy (Rappaz and Dantzig, 2009:425).

The TCP phases got negative effect on the properties of nickel based superalloys. The overall contents of chromium, molybdenum and tungsten promote the formation of topologically close-packed (TCP) phases, such σ,μ. The contents of the chemical elements in CMSX-4 Ni superalloy must be limited. Because of the disastrous potential consequences of such microstructures in spite of their beneficial effect on oxidation resistance or creep strength.

All heat treatment experiments for the nickel-based superalloy samples were performed in a laboratory-type vacuum heat treatment furnace. The furnace is equipped with a heating system of 80kW total power. The working chamber has a 600mm x 400mm x 400mm working area, and is equipped with a set of nine sleeve-protected thermocouples with a temperature measurement accuracy of 3°C. The heating process can be performed by convection to 950°C (in argon or helium atmosphere) or radiation to 1350°C (in vacuum). The furnace is equipped with a vacuum system consisting of a rotary and diffusion pumps, allowing a vacuum to $5 \cdot 10^{-5}$ bar.

Consequently, SC alloys in the solidified state cannot be used for the intended high temperature application. The solidus of polycrystalline alloys is below the γ'-solidus temperature, preventing the complete dissolution of γ' using solution heat treatment. The increased melting temperature of single crystal alloys frequently allows for refinement of the γ' microstructure with a solution annealing heat treatment followed by one or more aging

heat treatments. In alloys with a high volume fraction of γ and γ' eutectic after casting, the complete dissolution of γ' by the appropriate heat treatment is of extreme importance. Significant improvements in properties in equiaxed, columnar grained directionally solidified and single crystal superalloys are observed when increased levels of dissolution of the eutectic γ and γ' occurred during heat treatment. In addition to dissolving the eutectic γ and γ' and solutioning the γ' for subsequent reprecipitation, the solution heat treatment also reduces the chemical segregation of the elements. During solidification, some elements partition to the dendrite core, while other elements tend to accumulate in the interdendritic liquid and then solidify as the interdendritic and eutectic regions (Fuchs 2001:55).

Microsegregation can have either beneficial or deleterious effects on the properties of cast products. The microstructures has more uniform distribution of precipitates (or none at all) in order to obtain improved mechanical properties. The chemical inhomogeneity associated with microsegrigation usually leads to poor corrosion resistance. For these reasons, turbine blades are subject to a homogenization heat treatment, so as to reduce or eliminate residual segregation patterns, and solution treatment in order to re-dissolve non-equilibrium secondary phases produced by microsegregation.

The microstrucrure of CMSX-4 consists of γ matrix in which cuboidal γ' precipitates are embedded coherently. The volume fraction of γ' precipitates is typically about 70 %, the size of γ' cubes is about 0.4-0.5 μm and γ - γ' interfaces are aligned to 001 planes. This morphology itself indicates that the properties of superalloy single crystals are orientation dependent.

Table 5.3: Heat treatment schedule

Annealing: 1,277°C/4 h → 1,287°C/2 h → 1,296°C/3 h → 1,304°C/3 h → 1,313°C/2 h → 1,316°C/5 h/GFC*
Aging 1: 1,140°C/6 h/AC**
Aging 2: 871°C/20 h/AC**
* Gas furnace quench ** Air cooled

The solution heat treatment for this alloy is long and expensive, requiring almost a full day at elevated temperatures between 1277°C and 1316°C. Following this treatment, the material must be aged for an additional 26 hours.

The experimental observation of solution heat treatment for samples with withdrawal velocity of 3 mm/min were gained through metallography (SEM), crystal orientation assessment using the Laue method, and hardness tests.

After heat treatment, three sets of samples at different stages of the process were obtained:

1. Samples after annealing (see Figure 5.6);

2. Samples after aging 1 (see Figure 5.7);

3. Samples after aging 2 (see Figures 5.8, 5.9).

For investigation of the microstructure using SEM, the etchant H_3PO_4 with 10% solution of water was used. This etchant was prepared for electrolytic etching with the following parameters: voltage 3 V, amperage 0.2 A, time duration 3-5 s.

Figures 5.6…5.9 presents the heat treatment investigations.
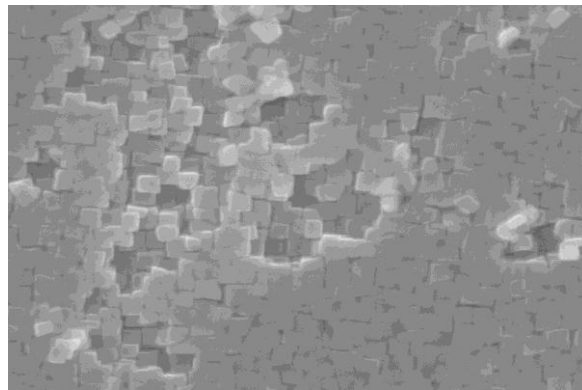
Figure 5.7: Sample after annealing.
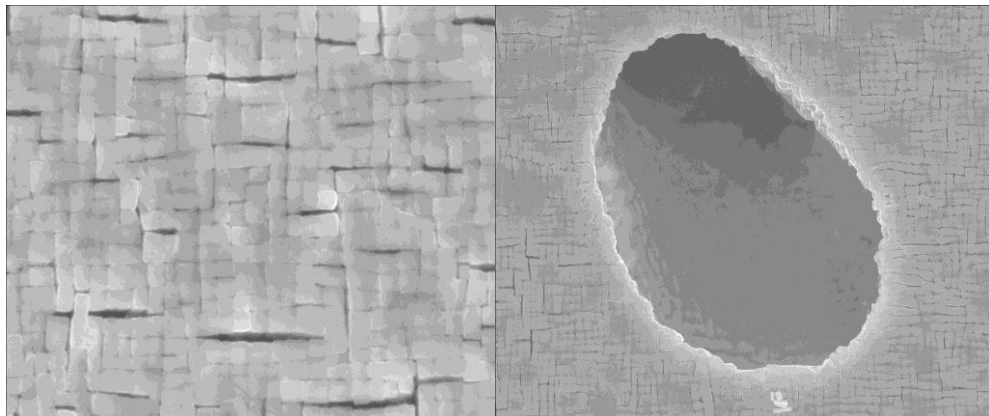
Figure 5.8: Sample aging 1 after 6 hours.
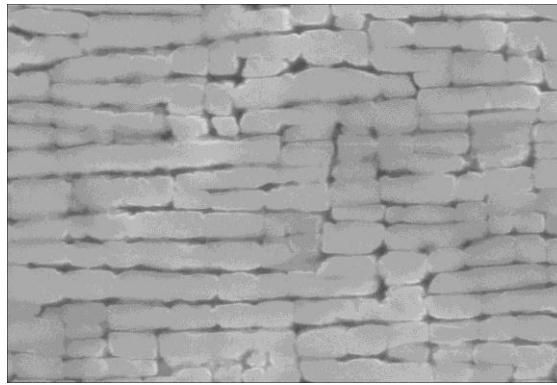
Figure 5.9: Sample aging 2 after 20 hours - dendrite core.
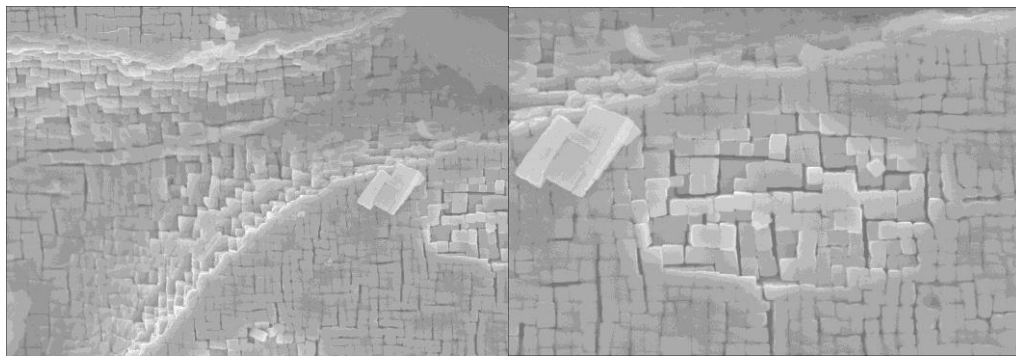
Figure 5.10: Sample aging 2.

Cast samples of CMSX-4 superalloy have a highly segregated, two-phase γ/γ′ microstructure. It is this chemical segregation that causes CMSX-4 to require a solution heat treatment. Through solution heat treatment of CMSX-4, the effects of segregation can be reduced. In addition to the solution heat treatment, one or more aging heat treatments are utilised to fully strengthen the material.

The first benefit of heat treatment is designed to homogenize the microstructure and reduce the effects of elemental segregation. The second benefit, through one or two aging heat treatments, is designed to develop a cuboidal γ/γ′ microstructure.

5.3. Mechanical properties

5.3.1 Hardness testing after heat treatment

Hardness testing was performed on samples of velocity 3 mm/min after three steps (solution heat treatment, aging 1 – 6 hours and aging 2 - 20 hours), under load of 0.5 kg.

Table 5.4: Hardness Hv (kg/mm^2)

Cast sample	Solution heat treatment	Aging 1	Aging 2
436	483	437	472

The hardness tests were carried out at different stages of heat treatment to observe how the hardness properties changed with heat treatment.

5.3.2 Creep testing

CMSX-4 alloy is used for high temperature applications because of its superior resistance to plastic deformation at elevated temperatures. The progressive (plastic) deformation of a metal at constant stress is called creep. The creep test measures the dimensional changes which occur from exposure to elevated temperatures, while the stress rupture test measures the effect of temperature on the long-term load–bearing characteristic.

Figure 5.11: Samples for creep test

Creep specimens with a diameter of 11.0mm, a uniform gauge section of 25mm and a total length of 70mm, were prepared according to the shape described in ASTM Test Methods E8 for round specimens. Creep strain test pieces of diameter 5.0 mm and gauge length 28 mm were machined from CMSX-4 single crystal material provided by Rzeszow University of Technology, in the form of 1 cm diameter cast rods. Creep strain testing was carried out using 4.87kN constant load creep testing machines; such testing was compliant with the British Standard UDC. Tests were performed in air at 982°C under constant loads, using a lever system and a three-zone furnace, according to the recommendations made in ASTM Designation E: 139 (Standard test methods for conducting creep, creep-rupture, and stress rupture tests of metallic materials).

The full load corresponding to the desired stress level was applied as quickly as was technically possible and then held constant until fracture or load removal time. An extensometer, capable of measuring strain with an accuracy of 0.0001 or better, was used to monitor the engineering strain of the specimen. The three attached thermocouples measured the temperature. The strain and the temperature were recorded during the entire test duration; the data was gathered rapidly during the load application time and the early creep period and at more infrequent intervals beyond the initial section of each test (as recommended by Sinha, 2006:130).

Figure 5.12: Creep machine W+b (Wolter + Bai) LFM2 =30kN.

The elongation creep equation is given by:

$$A_x = \Delta L/L_o \, 100\% \qquad\qquad (5.1)$$

where A_x – Elongation, %;

ΔL – Increase the gauge length, mm;

$$\Delta L = L_k - L_o, \text{ mm}, \qquad\qquad (5.2)$$

where L_o – Initial gauge length, mm;

L_k – Final gauge length after the test, mm.

The reduction in area is calculated using:

$$Z = [1 - (d_z/d_o)2] \, 100\%, \qquad\qquad (5.3)$$

where Z – Reduction of area, %;

d_o – Initial gauge diameter, mm;

d_z – Final gauge diameter at the fracture, mm.

Table 5.5: Creep Results for CMSX-4

Sample	Sample ID	Time to rupture (h)	Time to 1 % creep elongation (h)	Elongation creep, A_x %	Total % creep elongation	Reduc-tion of area, %	Measure-ment error %
1.1	P1/12/121/05	98.52	23.1	54.0	50	49.6	1.4
1.2	P1/12/121/06	82.37	18.6	66.7	55	50.7	1.4
3.1	P1/12/121/03	116.18	35.0	31.0	29	34.4	1.2
3.2	P1/12/121/04	126.52	38.9	44.2	36	42.5	1.3
5.1	P1/12/121/01	118.58	41.9	27.5	24	61.1	1.3
5.2	P1/12/121/02	102.34	31.2	34.3	32	59.0	1.3

Figure 5.13: Sample after creep test.

Creep testing investigation of single crystal structures is critical in understanding how a material will behave when subjected to a high-stress, high temperature environment. This is especially the case for turbine blade materials like CMSX-4.

The creep test results given in Table 5.4 indicates that the blade samples (3.1, 3.2) performed better than those from both the lower and higher withdrawal velocities. This implies the possibility of optimising the withdrawal velocity for SC castings.

For better creep properties, turbine blades castings are heat treated. For future research work, it will be necessary to analyse the extent of improvement of creep properties as a result of heat treatment, and the possibility of optimising costly heat treatment processes.

CHAPTER SIX: MICROSTRUCTURAL AND MACROSTRUCTURAL ANALYSIS

6.1   Analysis of Chemical Composition

6.1.1 Sample Preparation

For the investigations of microstructure and composition using SEM and OP, samples were prepared using standard metallographic procedures. In sequence, the steps include sectioning, mounting, grinding, rough polishing, final polishing, etching and microscopic examinations. All the steps for metallographic preparation are described in the sections below.

6.1.1.1 Sectioning

Sectioning, the removal of conveniently sized and representative specimen from a larger piece, is the first major operation preparation of metallographic specimens. On the surface, metallographic sectioning appears to be a type of machining process, although this is not the best way to consider metallographic sectioning.

The metallurgical cutoff saw consists of generally a consumable cutting wheel and the application of a coolant. An abrasive cutoff saw includes a high-speed motorized drive for a consumable, replaceable wheel. Each abrasive particle acts somewhat like a knife edge, scraping away a bit of material. The deformation associated with the scraping generates heat. If the water jet is properly aimed at the cut location, and an excessive amount of force is not applied, then the water cools the part as fast as the heat is generated, and the part is protected.

The most critical part of the cut is the last bit to separate, since it is difficult to get the coolant to the bottom of the cut. For the common fixture setups, a constant force will allow a noticeable increase in speed of cut just before the end. Slowing down as last bit of material is cut away helps to avoid local overheating (Vander Voort, 2007:324).

A series of free microsections were cut for each of three casting rods produced at different withdrawal velocities of 1 mm/min, 3 mm/min and 5 mm/min. The microsections were denoted in the order from the blade locking piece to its end, as 1.1, 1.2, 1.3 for rod No 1 as shown in Figure 6.2. The notation of the microsections for rods No 3 and No 5 (of withdrawal rates 3 and 5 mm/min respectively) were denoted in a similar way.

Figure 6.1: Casting rods for different withdrawal velocities for preparing samples.

(a)

(b)

Figure 6.2: a) Cutoff machine for samples b) Cross sections samples for rod 3.

Water alone should not be used as coolant for wet sectioning. A coolant should contain a water-soluble oil with a rust-inhibitor additive. This protects the moving parts of the cutoff machine, minimizes the possibility of burning, and produces better cuts.

6.1.1.2 Mounting

Mounting of the specimen is often desirable or necessary for subsequent handling and metallographic polishing, which occurs after the metallographic specimen is cut to an appropriate size.

Thermal–compression mounting with either thermosetting or thermoplastic compounds requires a temperature and pressure cycle in a mounting press in order to produce the desired mount. Mounting generally takes place by rapid heating of the specimen and

mounting material in a pressurized cylinder. The specimen is placed upside down on the bottom piston of the cylinder. The mounting material is poured over the specimen, and the top piston is placed inside the cylinder. Both heat and pressure are applied to the cylinder (Vander Voort, 2007:320).

Figure 6.3: Compression moulded mount.

6.1.1.3 Grinding

Water–cooled silicon carbide (SiC) paper at 220 – 240 rpm is most commonly used for grinding. Speed for grinding - 300 rev/min.

When proper metallographic abrasive blades have been used to section the specimen, so that cutting damage is minimal and the surface finish is optimal, grinding should commence with the finest possible abrasive. The coarser the abrasive, the greater the damage; a finer-size abrasive can be used for the grinding step. This removes the damage from cutting while imparting less damage than a coarse grit size grinding abrasive.

Figure 6.4: Grinding machine

6.1.1.4 Rough polishing

Polishing starts with 6-3 µm diamond abrasive. Speed for polishing -150 rev/min.

Diamond abrasives have replaced the use of 5 µm alumina (Al_2O_3) for rough polishing. The grinding step is usually followed by one or two further 9 µm diamond abrasive steps. A

lubricant/extender fluid, compatible with diamond abrasives, should be added to reduce friction and drag and to promote more efficient cutting.

Polishing should continue until grinding scratches are removed; 1-2 min is adequate. In an automated machine, the specimen rotates in the same direction to the platen. The faster the platen and head speed, the greater the centrifugal force, and the faster the abrasive is removed from the specimen. A second diamond polishing step follows, using a 3 or 1 µm diamond abrasive. This step is carried out in the same manner as the initial polishing. After each diamond polishing step, the specimen should be carefully cleaned to remove abrasive and extender oil.

Figure 6.5: Polishing machine

6.1.1.5 Final polishing

Final polishing involves one or more steps, depending on the need to remove all scratches. Polishing using 1 µm diamond finish may be adequate. Colloidal silica produces excellent results, but it is more difficult to use. The amorphous silica particles will crystallise if the solution evaporates. A polishing time of 1-2 min is usually adequate.The grinding and polishing speed effecting of quality surface specimen. The efficiency of grinding and polishing decreased the surface roughness. After polishing operation the surface must be high quality without scratches which can be difficult to investigate on OP or SEM.

6.1.1.6 Etching

Etching is used in metallography primarily to reveal the microstructure of a specimen under the optical microscope and scanning electron microscope. A specimen suitable for etching must include a carefully polished area of the material free of surface deformation and scratches.

Table 6.1: Microetchant for Ni superalloy for SEM investigation

Compositions	Comments
50 ml saturated aqueous	For nickel–based alloys: swab or immerse, room temperature.
25 g CuSO$_4$	
50 mL HCl	

Marble reagent consist CuSO4 (blue powder) for selectively dissolves the γ' microstructure.

For microstructural analysis of chemical compositions, 3 rods were used which were cut in 3 different cross sections for analysing the influence of velocity and temperature gradient. After preparation of the samples according to standard metallographic procedures, the samples were investigated using SEM.

6.1.2 Chemical compositions

Chemical composition for sample 3.1.

Chemical compositions were observed at different cross sections of sample at five points (Figure 6.6).
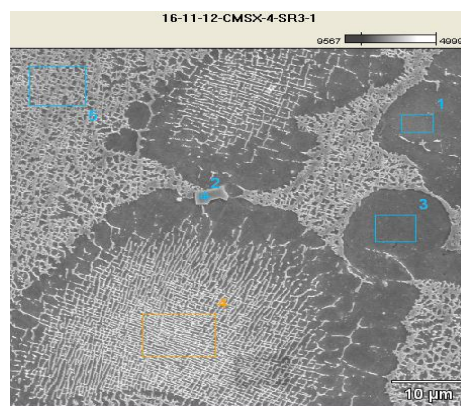
Figure 6.6: Chemical composition at five points of sample.

Figure 6.7 presents the results of the chemical compositions at each point (pt1…pt5).

Accelerating Voltage: 20.0 kV

Magnification: 2000
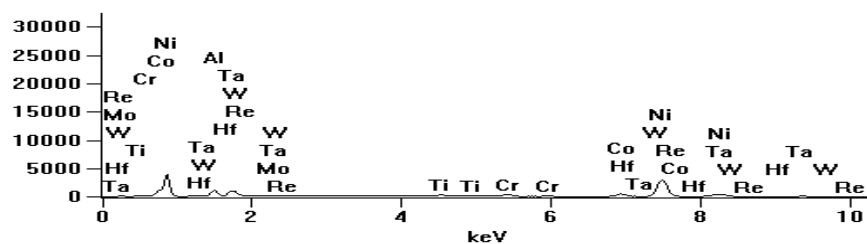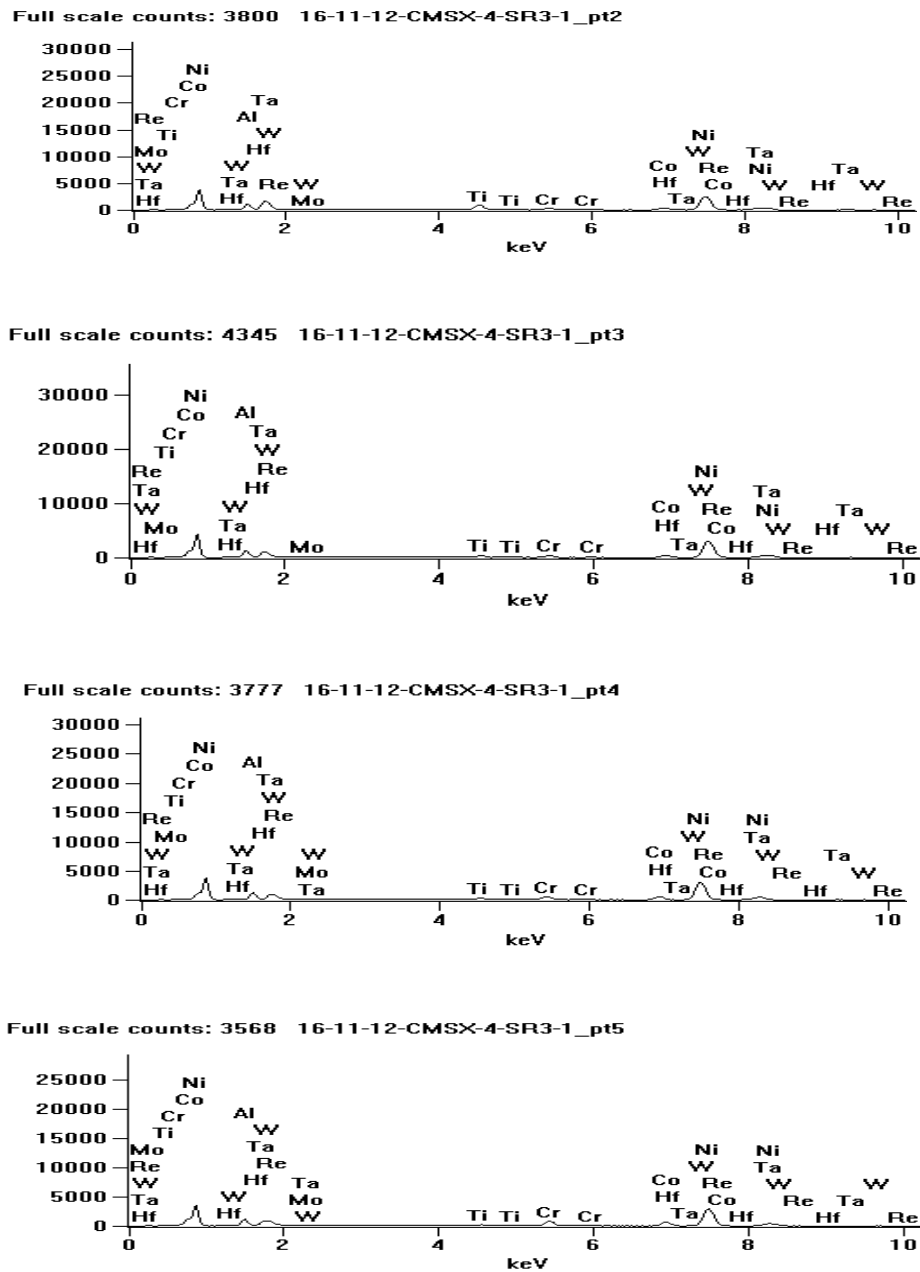
Figure 6.7: Chemical composition of sample 3.1 (v_w = 3 mm/min; section 1) (pt1…pt5).

Table 6.2: Chemical compositions for sample 3.1 wt. %

	Al	Ti	Cr	Co	Ni	Mo	Hf	Ta	W	Re
CMSX-4 pt.1	7.19	2.35	3.35	7.61	63.20	0.34	0.96	12.91	2.07	0.02
CMSX-4 pt.2	6.12	7.60	3.14	5.90	51.53	0.30	2.41	18.55	3.67	0.77
CMSX-4 pt.3	7.59	2.37	3.29	7.26	63.66	0.48	0.58	11.81	2.85	0.10
CMSX-4 pt.4	6.56	1.60	5.08	8.43	61.15	0.56	0.31	10.69	4.64	0.98
CMSX-4 pt.5	5.33	0.75	7.13	9.67	59.59	0.73	0.62	6.69	9.01	3.48

The chemical compositions (alloying elements in CMSX-4 given in Table 6.2) plays an important role in the final casting in providing specific mechanical properties such as

59

temperature, strength, toughness, and resistance to degradation in corrosive or oxidizing environments. In aeronautical applications in particular, in spite of their beneficial effect, the overall contents of chromium, molybdenum and tungsten must be limited; the more so, the larger the γ′ volume fraction, since these elements partition preferentially to the matrix. For single crystal structures, it is necessary to balance the alloy composition in order to avoid the formation of TCP phase.

6.1.3 Chemical composition at dendrite arm

Dendritic solidification leads to differences in composition, i.e. segregation, between the cores and surfaces of the dendrites, due to the rejection of solute into the liquid as the solid grows. The amplitude of segregation varies with the solute element concerned, depending on the corresponding value of the partition coefficient between the solid and liquid. Also, the amplitude of the segregation depends on the conditions of solidification and cooling. It is a maximum when solidification is rapid, since there is less time for diffusional exchanges at the solid/liquid interface (Durand-Charre, 1997:60).

According to Figures 6.8…6.9, the chemical compositions of Ni and alloying additions at the dendrite core and surface (arm) are different.
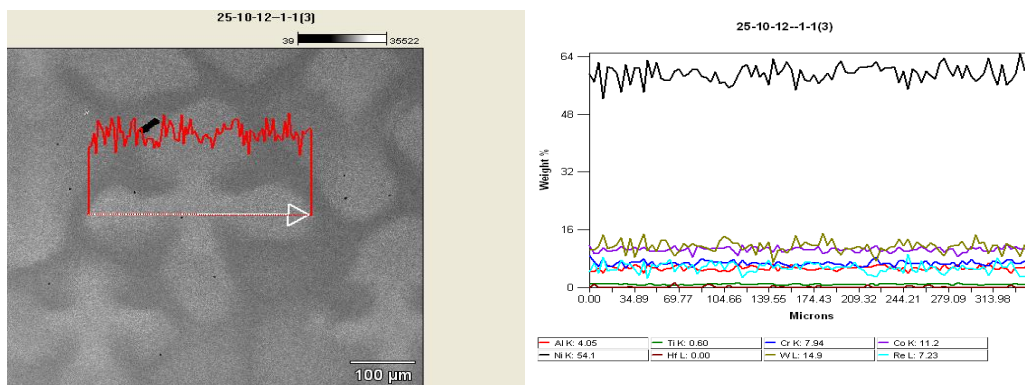
Figure 6.8: Chemical composition of alloying elements at dendrite arm.
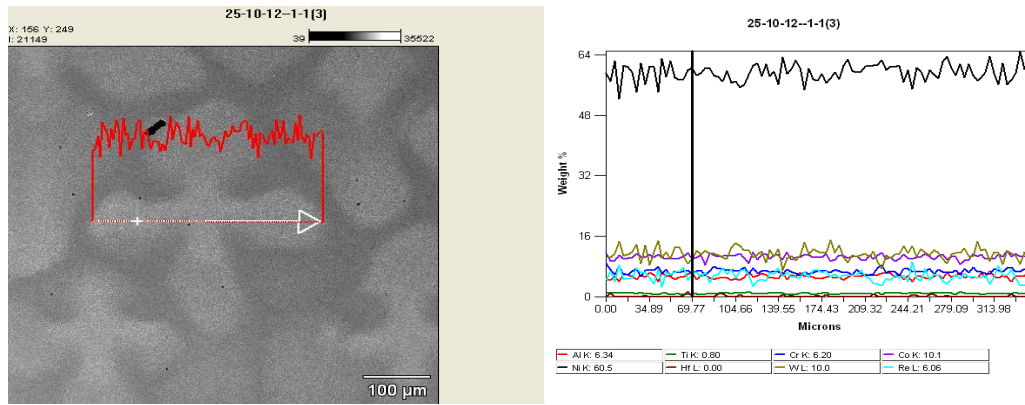
Figure 6.9: Chemical compositions at second point.
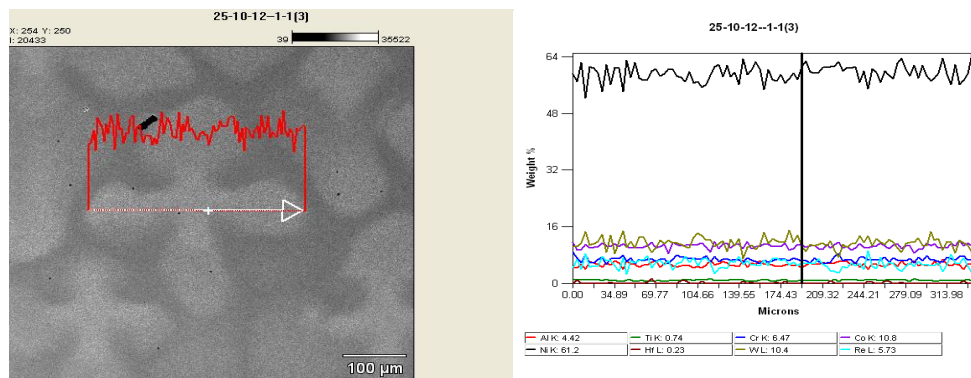
Figure 6.10: Chemical compositions at third point.

6.2 Analysis of Dendritic Crystal Structure

6.2.1 Introduction

The dendritic structure of CMSX-4 consists of compositional variation such as the primary (PDA), secondary (SDA), and tertiary dendrite arms containing less alloying or impurity elements than interdendritic regions. The chemical composition of superalloys changes at interdendritic regions and dendritic arms. The condition of creating in interdendritic regions a two-phase structure arises when alloying elements or impurity content is high.

6.2.2 Electrolytic etching

In electrolytic (anodic) etching, electrical potential is applied to the specimen using an external circuit. The typical setup consists of the specimen (anode) and its counterelectrode (cathode) immersed in an electrolyte. Positive metals ions leave the specimen surface and diffuse into the electrolyte; an equivalent number of electrons remain in the material. Specimen dissolution without formation of a precipitated layer occurs in this instance. Three samples at cross sections 1.1, 3.1 and 5.1 for different velocity ware electrolyticaly etched for observing microstructure using SEM.

Single crystal nickel-based superalloys reveal a two phase microstructure consisting of a solid solution hardened Ni-based γ matrix (volume fraction ≥30%) and γ′ precipitates. A high volume fraction of coherently precipitated γ′- cubes is separated by thin channels of γ-matrix. The γ and γ′ phases do not have the same chemical composition and crystallographic structure (the γ′ phase has a primitive cubic ordered, Ni_3 (Al)-based structure, while the γ phase has a face-centered cubic (FCC) Ni-based, disordered structure). In the undeformed condition, the cuboidal γ′ precipitates are coherently embedded in the γ matrix. At high temperature and applied stress the γ/γ′ microstructure becomes unstable: the initially cuboidal γ′ precipitates often coalesce into rafts which are oriented perpendicular to the direction of the tensile stress. The microstructure of the microsections ware observed (as-cast samples) using a Hitachi S-3400N electron scanning microscope with EDX and Nikon Epiphot 300 light microscope.

Figure 6.11: Sample inside the SEM.

6.2.3 Results after experiment using SEM

The Figures 6.12…6.14 shows the dendritic structure after casting for withdrawal rates (1, 3 and 5 mm/min).
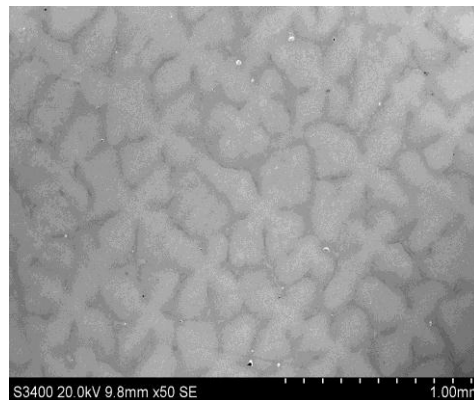
Figure 6.12: Dendritic structure for sample 1.1.
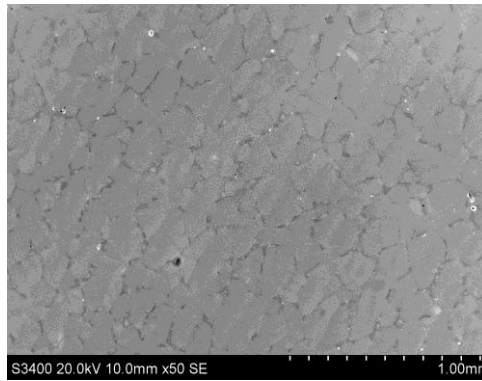
Figure 6.13: Dendritic structure for sample 3.1.
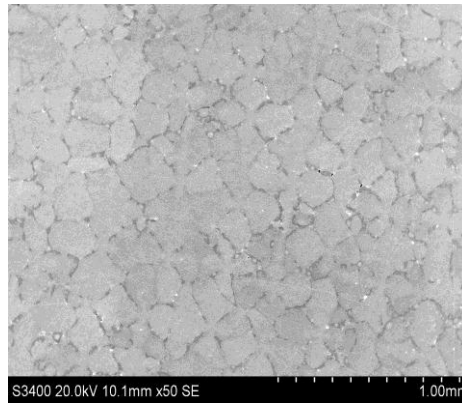
Figure 6.14: Dendritic structure for sample 5.1.

The microstructure of the multicomponent alloy is dendritic, but its basic component γ'-phase crystals are arranged in an ordered way. As a result, Laue diffraction patterns are the same as for single-phase γ'-phase single crystals. The formation of such single crystal structures consists of the growth of dendrites in the three orthogonal crystallographic orientations of the [100] type (see Section 5.1.3). For all dendrites, one of these directions, usually denoted as the [001]γ', is parallel to the growth direction of the structure (Onyszko et al, 2010:1328).

6.2.4 Microstructure investigation, using OP

In this Section, microstructure of the samples previously investigated using SEM are now investigated using a Nikon Epiphot 300 optical microscope.

Table 6.3: Microetchant for Ni superalloy for OP investigation

Compositions	Comments
33 mL CH_3COOH	For nickel–based alloys: swab or immerse, room temperature.
33 mL H_2O	
33 mL HNO_3	
1 mL HF	

From the OP micrographs shown in Figures 6.15…6.17, it can be seen that the final microstructure and, hence, properties of the CMSX-4 superalloy samples are very sensitive to the thermal conditions present during solidification.

Solidification is dendritic in character, and the primary (L_1) and secondary dendrite arm spacings are dependent on the cooling rate (a function of withdrawal velocity R and thermal gradient G).
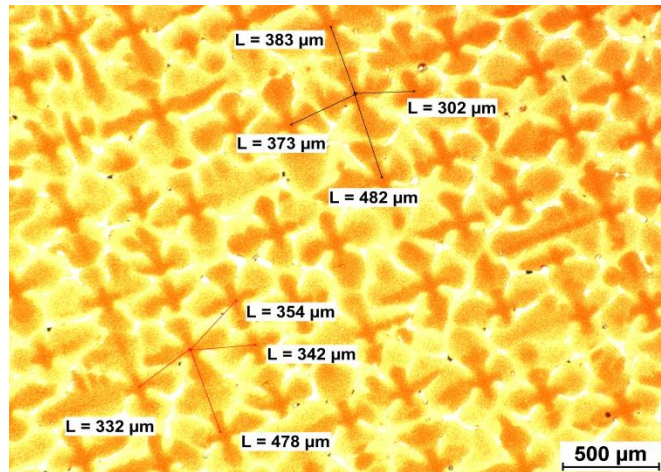
Figure 6.15: Microstructures of sample 1.1.
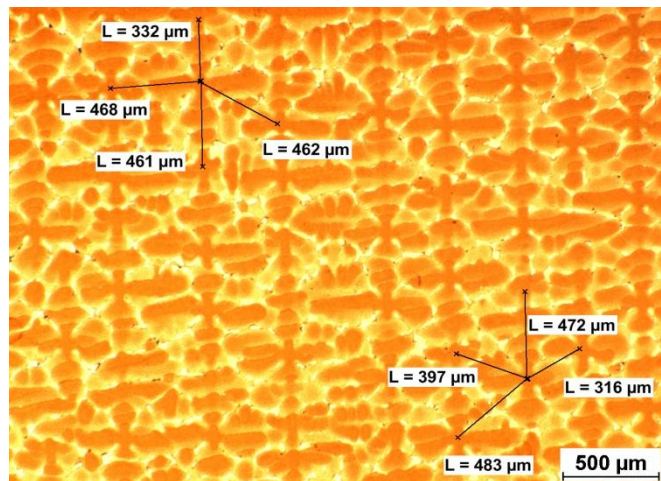
Figure 6.16: Microstructure of sample 3.1.
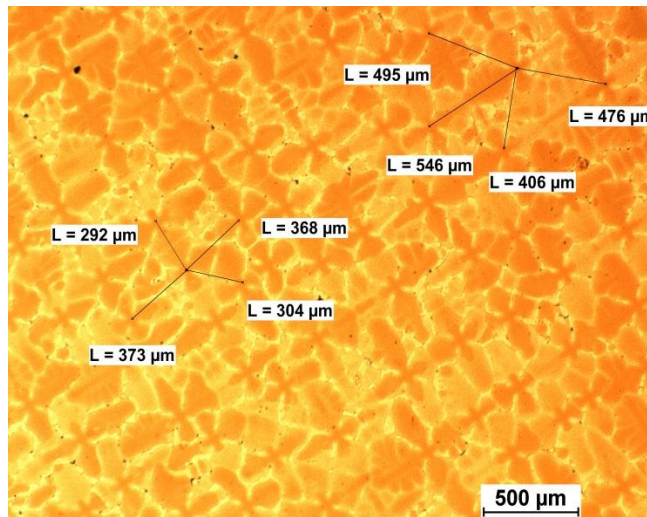
Figure 6.17: Microstructure of sample 5.1.

For columnar grains, the spacing between the primary trunks L_1 (Figures 6.15…6.17) were measured. The measurements were carried out for 2 dendrites each with 4 points, and then averaged.

Table 6.4: Dendritic spacing for samples

Sample ID	Average distance L, μm
Velocity -1 mm/min	
1.1	380.75
1.2	425.63
1.3	430.25
Velocity - 3 mm/min	
3.1	423.90
3.2	549.50
3.3	418,75
Velocity - 5 mm/min	
5.1	407.50
5.2	454.25
5.3	473.88

For the all experimental conditions investigated, the optimum withdrawal rate that gives the most refined, homogeneous microstructure was found to be 3 mm/min. The increase of withdrawal velocity (5 mm/min) increases the thermal gradient and generates lateral overgrowth of secondary arms and other grain defects.

It is noted that modelling of the solidification process at various withdrawal rates revealed significant differences in thermal gradient magnitude and direction of the solid-liquid interface, resulting in differences in the predicted dendrite arm spacing for the SC process.

6.3　Microprobe analysis of segregation

Cast CMSX-4 is highly segregated, which is a large contributor to the need for a solution heat treatment.

One method to analyse the degree of segregation is through microprobe analysis. The analysis was conducted on an as-cast metallography sample. This sample was observed in the polished and etched condition. Three types of microstructural regions were examined to determine local concentrations of alloying elements: dendrite cores, eutectic regions, and the interdendritic region. Five different representative sites for each of the three regions were selected for analysis. From the composition data, partitioning coefficients of the alloying elements can be determined. The partitioning coefficient, k′ = (dendritic composition)/(interdendritic composition), indicates how strongly a given element segregates to either the dendrite or the interdendritic regions. The higher the partitioning coefficient, the higher the concentration of a given element in the dendrite core region. Conversely, the lower the partitioning coefficient, the lower the concentration of a given element in the dendritic region with respect to the interdendritic region (Wilson 2003:36).

As an example, the weight percentage of W in a dendrite of as-cast CMSX-4 is 1.94 times as great as the weight percentage of W in the interdendritc region.

Table 6.5: Average compositions of CMSX-4 dendritic core and partitioning coefficients for sample 3.1 (in wt.%)

	Ni	Al	Ti	Cr	Co	Mo	Hf	Ta	W	Re
Average composition	60.31	6.03	1.56	5.19	8.57	0.54	0.63	10.09	5.24	1.49
Dendrite core	56.59	5.33	0.75	7.13	9.67	0.73	0.62	6.69	9.01	3.48
Interdendritic area	63.20	7.19	2.35	3.35	7.61	0.34	0.96	12.91	2.07	0.02
Eutectic area	61.15	6.56	1.60	5.08	8.43	0.56	0.31	10.69	4.64	0.98
Partitioning coefficient	0.92	0.81	0.15	1.40	1.15	1.30	2.00	0.63	1.94	3.55
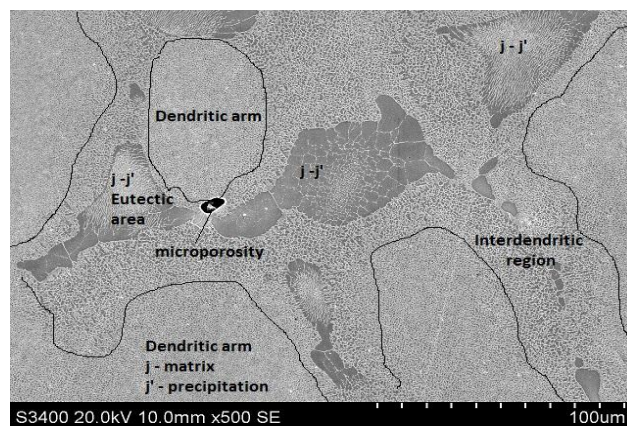
Figure 6.18: SEM micrographs of dendrite morphology CMSX-4

66

The dendritic solidification of CMSX-4 leads to differences in chemical composition (segregation) between the dendritic core and surface of the dendrites, due to the rejection of solute into the liquid as the solid grows. The amplitudes of the segregation are presented through the values of the partition coefficients between the solid and liquid (as shown in Table 6.5 and Figure 6.18).

In CMSX-4 superalloy, the alloying elements like Co, Cr, Re and W segregated at the dendritic core with Al, Ni, Ta and Ti partitioning to the interdendritic regions. The heavy Re, Ta and W segregated particularly strongly. The partitioning coefficients (k′) of these elements are presented in Table 6.5. Note that the elements which segregated to the dendrite cores during solidification have partitioning coefficients greater than unity. The greater the partitioning coefficient, the greater the degree of segregation. A partitioning coefficient less than unity indicates that the element segregated to the liquid during solidification, ultimately solidifying in the interdendritic region. The smaller the partitioning coefficient, the stronger the degree of segregation during solidification (Fuchs 2001:55).

6.4   Macrostructural analysis of casting surface
6.4.1 Introduction
The benefits of SC as opposed to conventionally cast and DS components critically depends on avoiding the introduction of casting defects, such as stray grains, freckles, or deviations from the required crystal orientation. The macrostructural investigation of casting surfaces of turbine blades showed growth of dendritic structure from starter blocks and the passing of one crystal through the grain selector (Figure 6.19).

6.4.2 Macroetching for CMSX-4
Macroetching of cast specimens is generally performed as a research tool to study the solidification characteristics. Features observed on macroetched cast turbine blades and casting rods depict the results of solidification. Near the surface, the grain structure will be finer than elsewhere. Dendrites will be visible, with the primary axis in the solidification direction. Segregation and shrinkage cavities may also be observed. Porosity due to gas evolution, however, is unlikely to be observed.

Figure 6.19: Macrostructural analysis for turbine blades and casting rods at velocity 1; 3; 5 mm/min.

6.4.3 Results

Macrostructural analysis was conducted to examine casting defects on the surfaces of the turbine blades and casting rods. This also provides the opportunity to observe the nucleation and crystal growth (competition growth dendrites) in the starter blocks.
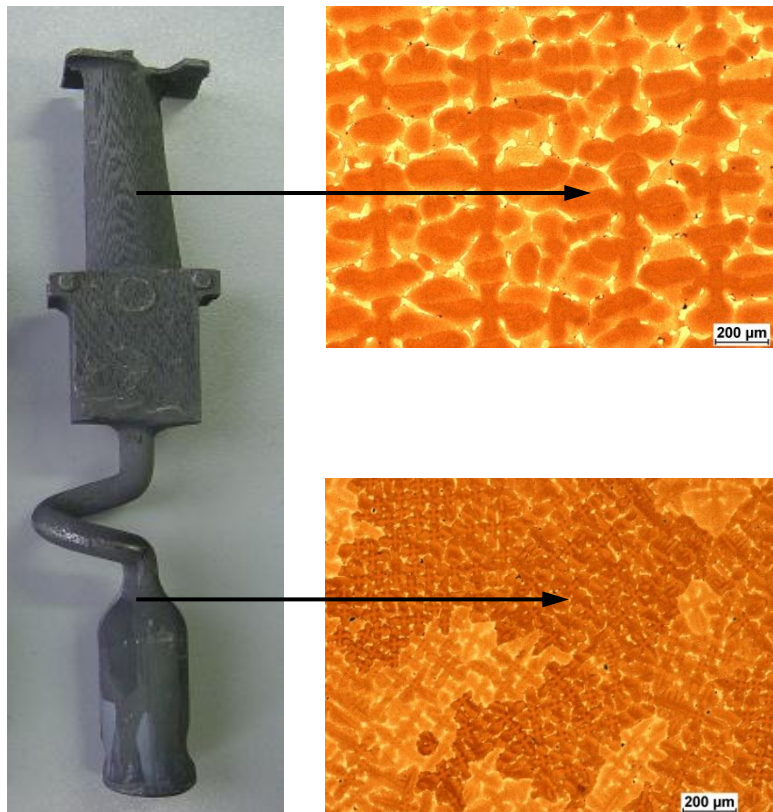
Figure 6.20: Macrostructural analysis for turbine blade (crystal structure at starter block and dendritic structure at blade).

Figure 6.20 represents the grain boundaries, which were determined on the basis of the misorientation between dendrites. The great portion of the grains grown from the starter block disappeared when going through the grain selector, and only a few passed this region (Seo et al, 2009:394).

The best macrostructural results were found in the case of withdrawal velocity 3 mm/min. At 1 mm/min and 5 mm/min, casting defects were discovered such as sliver, new grains on the surface of the blade, and freckles. Freckle formation (withdrawal rate 1 mm/min) is promoted by low cooling rate (low thermal gradients) and corresponding large dendrite arm spacing for specific alloy composition. Freckles are enriched in elements to segregate to the interdendritic area during the solidification process.

Other casting defects are sensitive to the details of casting geometry and casting process parameters, and less sensitive to the alloy chemistry. These defects may limit mechanical properties and are also controlled in specifications and monitored inspection approaches.

CHAPTER SEVEN: CONCLUSIONS AND RECOMMENDATIONS

7.1 Conclusions

This research work was the first attempt in the South African foundry industry to study the effect of spiral design on single crystal (SC) turbine blades. The simulation and experimental results revealed that the spiral (grain selector) can be used to effectively select one grain for single crystal blades.

By comparing the simulated results with experimental observations, it is proposed that the shape of the spiral grain selector for turbine blades be selected by geometrical control mechanism. Therefore, the design (shape and dimension) of turbine blades can make a significant contribution to the improvement of the productivity for single crystal casting industry.

The analysis of the numerical simulation and experimental research results was used as a basis for verification and selection of nucleation parameters, grains growth rate as well as boundary conditions applied during the simulation of directional solidification process performed using the Bridgman method. Results from the numerical simulations made it possible to establish the temperature field in the heating chamber of the furnace, the ceramic shell mould and the cast. It formed the basis for determining the undercooling of liquid alloy. The undercooling value calculated in the simulation process was applied in the CAFE module (ProCAST simulation software) in order to simulate the grain growth in the cast.

Through ProCAST, it was possible to characterise the solidification process and predict the grain microstructure of turbine blades produced from CMSX-4, depending on the technical (material and process) parameters.

The microstructure and creep behavior of the SC castings is impacted by the applied heat treatment process. The heat treatment of the second generation, single crystal superalloys, CMSX-4 requires approximately 45 hours with heating temperature up to 1316°C. The cost of solution heat treatment is very significant.

The aim of the heat treatment is to dissolve both precipitating phases of γ' formed during solidification, as well as the eutectic γ'/γ phase to reduce the chemical segregation of some elements at the dendritic core and interdendritic areas. It was shown that the solution heat treatment resulted in the elimination or reduction of the segregation to produce a more uniform, homogeneous microstructure.

Macrostructural analysis was conducted to examine possible casting defects on the surfaces of the turbine blades and casting rods at different withdrawal rates. This also

provided the opportunity to observe the nucleation and crystal growth (competition growth dendrites) in the starter blocks. The macrostructural analysis undertaken clearly showed how the withdrawal velocity affected the crystal structure of turbine blades.

The main concern of CMSX-4 alloy is the definition of specification limits for acceptable range of individual alloying elements, in particular the avoidance of a class of phases such as topologically close packed phases (TCP). TCPs are detrimental because they deplete strengthening elements from the microstructure and/or serve as crack-initiation sites during cyclic loading of turbine blades.

The amplitude of the segregation for the single crystal structures was investigated through calculation of the partition coefficient. The amplitude of the segregation depends on the solidification process parameters and subsequent cooling rate. It was found to be a maximum when the solidification was rapid (5 mm/min withdrawal velocity), since there is less time for diffusional exchanges at the solid/liquid interface.

Overall, this study has shown that the withdrawal velocity in the Bridgman process for SC castings influences the quality of the castings, and that there exists optimum control parameters for the solidification of such castings.

7.2   Recommendation for future research work

Based on the results of the research project and conclusions, the following recommendations are made for future research work.

Creep investigation of SC castings:

After initial creep tests, it was found that different samples from the same casting rod displayed different creep properties. Further creep investigations are therefore necessary to establish the creep properties at different points along a SC casting. Furthermore, it is known that heat treatment improves the creep properties of SC castings (due to improvements in microstructure as discussed in this study). A comparative investigation of heat treatment properties before and after heat treatment is therefore recommended.

Optimisation of Ceramic Shell Thickness:

It is realised that the ceramic shell can affect the quality of the final cast, especially in terms of casting defects on the surface of blades. It is therefore recommend that investigations on the use of ceramic shell models be undertaken in order to optimise shell thickness and shell layer materials.

Improved Heat Transfer during Solidification:

A new approach for future research involves increasing the thermal gradient during solidification through the use of liquid-metal coolants (LMCs) during the solidification process. It is understood, from modeling and simulation, that this will provide better mechanical properties (strengthening) of turbine blades. Experimental trials are needed to validate the predicted results and to provide guidelines for industry to explore this new technique.

REFERENCES

1. Alexandrou, A., 2001. Principles of fluid mechanics, Pinntice-Hall.

2. Askeland, D.R., Fulay, P.P., Wright, W.J., 2010. The science and engineering of materials. Copyright.

3. Bidwell, H. T., 1969. Investment Casting. Brighton, Machinery Publishing.

4. Beeley, P., 2011. Foundry Technology. Butterwoth Heinemann, Oxford.

5. Brand, D. A., Warner, J.C., 2005. The Goodbeart_Willoox Company.

6. Callister, W. D., Rethwisch, D. G., 2011. Material science and engineering.

7. Campbell, J., 2003. Casting, Elsevier Ltd.

8. Campbell, F.C., 2006. Manufacturing Technology for Aerospace Structural Materials, Elsevier Ltd.

9. Dantzig, J.A., Rappaz, M., 2009. Solidification. Engineering sciences EPFL Press.

10. Edited by Davis, J.R., 1997. ASM specialty hand book. Copyright.

11. Dieter, G.E., Bacon, D., 1988. Mechanical Metallurgy. Mcgraw-Hill Book company.

12. Durand-Charre, N., 1997. The Microstructure of Superalloys Gordon and Breach science publishers. Copyright OPA (Overseas Publishers Association).

13. Fredriksson H., Akerlind, V., 2006. Material Processing during casting.

14. Hattel, J., 2005. Fundamentals of numerical modeling of casting process.

15. Hosford, W. F., 2007. Metal forming mechanics and metallurgy. Cambridge.

16. Kurz, W., Fisher, D.J., 1998. Fundamental of solidification. Zurich, Switzerland, Trans Tech.

17. Kutz, M., 2006 Mechanical Engineers' Handbook, Energy and Power. John Wiley & Sons.

18. Mohanty, A.K., 2009. Rate processes in metallurgy. PHI Learning Private Limited.

19. Reza &Lara Abbaschian, Reed-Hill, R., 2010. Physical Metallurgy principles.

20. Reed, R.C., 2006. The superalloys fundamentals and applications. Cambridge university press.

21. Vander Voort, G. F., 2007. ASM Handbook, Metallography and microstructures. Volume 9. Copyright.

22. Edited by Sims, C. T., Stoloff, N. S., Hagel, W. C., 1987. SUPERALLOYS II high temperature materials for aerospace and industrial power John Wiley &Sons, Inc.

23. Tamarin, Y., 2002. Prospective coatings for turbine blades. Copyright by ASM International.

24. Prof. Beckermann, C., Dr Boettinger, W.J., Prof. Combeau, H., Prof. Dantzing, J., Prof. Ludwig, A., Prof. Rappaz, M., 2011. Solidification course 2011. Les Diablerets, Switzerland, Copyright CALCOM ESI SA.

25. Dong, H. B., 2007. Analysis of grain selection during directional solidification of gas turbine blades. Proceedings of the World congress on Engineering 2007, 2-4 June . London, U.K.:1-6.

26. Onyszko, A., Kubiak, K., Sieniawski, J. 2009. Turbine blades of the single crystal nickel based CMSX-6 superalloy.Journal of achievements in materials and manufacturing engineering, 32(1):66-69, January.

27. Dedmon, L. S., Pilch, J., Dutler, S., Galbraith, J. 2008. Simulation of Solidification of 19 inch Diameter, Double Length Still Ingot. Proccedings of the 2008 Fall Conference of the ASME Rail Transportation Division RTDF2008, September 24-25, 2008, Chicago, Illinois USA:1-4.

28. Egner-Walter, Dr.-Ing. A., Olive, S., no date. Using Stress Simulation to tackle Distortion and Cracking in Castings. MAGMA GmbH, Germany, Maxima Engineering, UK:1-13.

29. Mirbagheri, S.M.H, Dadashzaden, M., Serajzadeh, S., Taheri, A.K., Davami, P. 2004. Modeling the effect of mould wall roughness on the melt flow simulation in casting process. Mathematical Modeling. 28:933-956, May 6.

30. Li, D.Z., Campbell, J., Li, Y.Y. F. 2004. Filling system for investment cast Ni-base turbine blades. Journal of Materials Processing Technology, 148:310-316, February 11.

31. Wang, J. P., Borthwick, A.G.L. 2003. Finite-volume type VOF method on dynamically adaptive quadree grids. International journal for numerical methods in fluids, 00:1-22.

32. Hirt, C. W., Nichols, B. D., 1979. Volume Fluid (VOF) Method for the Dynamics of free Boundaries. Journal of computational physics, 39:201-225, November 1.

33. Cleary, J.HA. P., Alguine, V., Nguyen, T., 1999. Simulation of die filling in gravity die casting using SPH and MAGMASOFT. Second International Conference on CFD in Minerals and Process Industries, 6-8 December, Australia: 423-428.

34. Dong, Y., Bu, K., Dou, Y., Zhang, D. 2011. Determination of interfacial heat-transfer coefficient during investment casting process of single-crystal blades. Journal Materials Processing Technology, 211:2123-2131, July 28.

35. Carter, P., Cox, D. C., Gandin, C.A., Reed, R.C., 1999. Process modeling of grain selection during the solidification of single crystal superalloy castings. Material Science and Engineering, A280:233-246, October 11.

36. Sturm, Dr.-Ing. J.C., Busch, Dipl.-Ing. G., 2010. Cast-iron a predictable material. World Foundry Congress , China:16-20.

37. Pahmaty, S., Reza, R. M,. Javad, A., 2009. Design and Manufacture of Wax Injection Tol for Investment Casting Using Rapid Tooling. Tsighua science and technology 14(S1):108-115, June.

38. Hahn, Dr.Ing.I, Hartmann, Dr.-Ing. G., 2008. Automatic compututerized optimization in die casting process. Casting Plant & Technology 4:2-14.

39. Theodorakakos, A., Bergeles, G., 2003. Simulation of sharp gas-liquid interface using VOF method and adaptive grid local refinement around the interface. International journal for numerical methods in fluid 45:421-439, November 15.

40. Grozdanic, V., 2009. Finite-difference methods for simulating the solidification of casting. Materials and technology 43(5):223-237, May 12.

41. Shepel, S. V., Paolucci, S., 2002. Numerical simulation of filling and solidification of permanent mold casting. Thermal Engineering 22:229-248, June 21

42. Sietmaz, L.E., Bolster R.N., Singer I.L. 1999. IBAD MoS_2 lubrication of titanium alloys. Naval Research Laboratory, Washington, DC 20375-5000, USA, June 30.

43. Meng, X., Li,J., Jin, T., T., Sun, X., Sun, C., Hu, Z., 2011. Evolution of grain selection in spiral selector during directional solidification of nickel-base superalloys. Elsevier, Journal Materials Science Technology 27(2):118-126, October 13.

44. Pavel, P. M., Ene, N., 2003. Planar solidification solution with mushy zone. Journal Energy Conversion and Management, 44:2977-2989, January 28.

45. Wang, H., Liu, F., Yang, G., Zhou, Y., 2010. Modelling the overall solidification kinetics for undercooled single-phase solid-solution alloys. II. Model application. Journal Acta Materiaia, 58:5411-5419, July13.

46. Hou, N.X., Wen, Z.X., Yue, Z.F., 2009. Creep behavior of single crystal superalloy specimen under temperature gradient condition. Journal Materials Science and Engineering A, 510-511:42-45, April 3.

47. Zhao, X., Liu, L., Yu, Z., Zhang, W., Fu, H., 2010. Microstructure development of different orientated nickel-base single crystal superalloy in directional solidification. Journal Materials characterization, 61:7-12, September 24.

48. Galantucci, L.M., Tricarico, L., 1998. A computer-aided approach for the simulation of the directional-solidification process for gas turbine blades. Journal of Materials Processing Technology 77:160-165.

49. Wang, W., Kermanpur, A., Lee, P.D., Mclean, M., 2003. A Model Of Solidification Microstructures In Nickel Based Superalloys: Predicting Primary Dendrite Spacing Selection. Journal of materials Science 38:4385-4391.

50. Dai, H. 2008. A study of solidification structure evolution during investment casting of Ni-based superalloys for aero-engine turbine blades. PhD thesis, University Leicester.

51. Yang, X. L., Dong, H.B., Wang, W., Lee, P.D., 2004. Microscale simulation of stray grain formation in investment cast turbine blades. Journal Materials Science and Engineering A 386:129-139, July 2.

52. Panwisawas, C., Mathur, H., Gebelin, J-C., Putman, D., Rae, C.M.F., Reed, R.C., 2012. Prediction of recrystallization in investment cast single-crystal superalloy. Journal Acta Materialia, September 5.

53. Gandin Ch-A., Rappaz, M., 1194. A coupled finite element-cellular automaton model for the prediction of dendritic grain structures in solidification process. Journal Acta Metal Material 42(7):2233-2246, January 10.

54. Brundidge, C.L., Vandrasek, D., Wang, B., Pollock, T.M. 2011. Structure Refinement by a liquid metal cooling solidification for single-crystal nickel-base superalloy. Journal The Mineral, Metals& Material society and ASM International 43 A:965, October 27.

55. Gao, S. F., Liu, L., Wang, N., Zhao, X.B., Zhang, J., Fu, H.Z., 2012. Grain selection during casting Ni-base, single –crystal superalloy with spiral grain selector. Journal The Mineral, Metals& Material society and ASM International 43 A:3767, April 11.

56. Bhadeshia, H. K. D. H., Nickel Based Superalloys, http://www.msm.cam.ac.uk/phasetrans 2003/Superalloys/superalloys.html, Cambridge, University of Cambridge.

57. Hillier, G. S., Rae, C. M. F., Bhadeshia, H. K. D. H.1988. "Extrinsic and Intrinsic Nodes in the Gamma Prime Phase of a Single-Crystal Superalloy" Acta Materialia, 36: 95.

58. Zhou, Y. Z., Volek, A. and Green, N. R. 2008. "Mechanism of Competitive Grain Growth in Directional Solidification of a Nickel-Base Superalloy." Acta Materialia 56(11): 2631.

59. Chilton, R. A. 2002. Experimental Study and Modelling of the Cell-Dendrite Transition. Ph. D., Oxford, University of Oxford.

60. Merihanage, W. U.,Huijuan, D., Dong, H., Browne, D. J. 2013. "Computational Modeling of Columnar to Equiaxed Transition in Alloy Solidification." Advanced Engineering Materials 15(4):216-229.

61. Duffy, M.O., Morris, P.M., Mador, R.J. 1998. "Casting solidification analysisand experimental verification." Finite Elements in Analysis and Design 4(1):1-7.

62. Dong, H.B., Lee, P.D., 2005. "Simulation of the columnar-to equiaxed transition in directionally solidified Al-Cu alloys." Acta Materialia 53(3): 659-688.

63. Seo, S-M., Kim, I-S., Lee, J-H., Jo, C-Y., Miyahara, H., Ogi, K. 2009. "Grain structure and texture evolutions during single crystal casting of the Ni-base superalloy CMSX-4."Metals and Materials International 15(3) 391-398.

64. Hegde, S.R., Kearsey, R.M., Beddoes, J.C., 2010. "Designing homogenization-solution heat treatment for single crystal superalloys." Materials Science and Engineering 527(21-22):5528-5538.

65. Fuchs, G.E., 2001. "Solution heat treatment response of a third generation single crystal Ni-base superalloys." Materials Science and Engineering 300(1-2):52-60.

66. Wilson, B.C., 2003. "The effect of solution heat treatment on a single-crystal Ni-based superalloys." JOM 55(3) 35-40

67. Sinha, N.K., 2006, "Constant-load tertiary creep in nickel-base single crystal superalloys. " Materials Science and Engineering 432(1-2):129-141.

APPENDIX A: MICROSTRUCTURE INVESTIGATION USING SEM

A1:   Chemical composition of sample 1.1

Accelerating Voltage: 20.0 kV

Magnification: 2000

For analysing chemical composition at 6 points of sample:

Full scale counts: 2292   16-11-12-CMSX-4-SR1-1_pt3

Full scale counts: 3988   16-11-12-CMSX-4-SR1-1_pt4

Full scale counts: 3657   16-11-12-CMSX-4-SR1-1_pt5

Full scale counts: 3125   16-11-12-CMSX-4-SR1-1_pt6

79
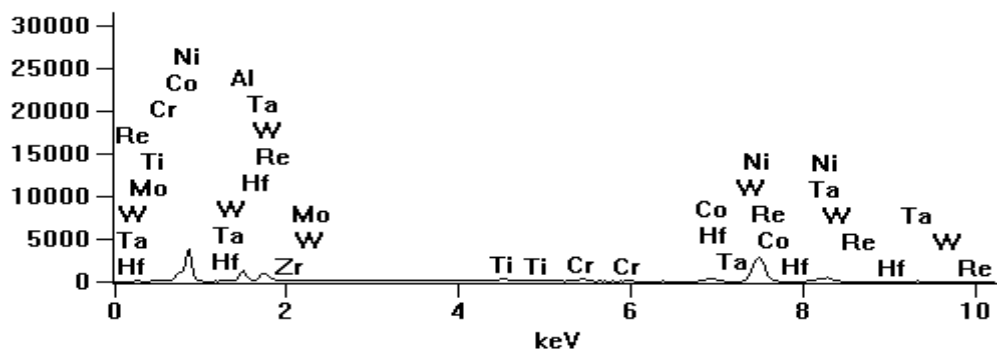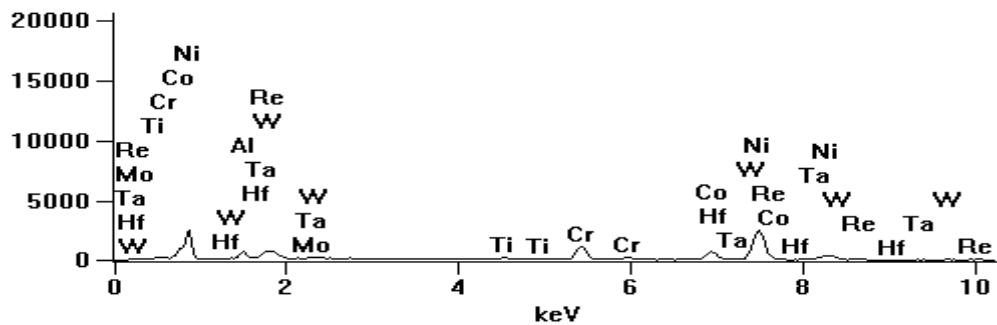
A2: Chemical composition of sample 1.1

	Al	Ti	Cr	Co	Ni	Mo	Hf	Ta	W	Re
CMSX-4 pt.1	6.78	2.00	2.56	6.92	60.18	0.41	1.77	14.50	4.61	0.28
CMSX-4 pt.2	3.36	1.01	11.04	11.31	50.69	1.18	0.82	4.85	9.38	6.35
CMSX-4 pt.3	0.76	1.13	2.32	7.33	71.03	0.03	2.68	10.57	3.01	1.31
CMSX-4 pt.4	7.39	2.04	3.29	7.48	64.30	0.45	0.00	9.16	4.99	0.90
CMSX-4 pt.5	6.08	1.30	5.75	8.42	60.08	0.46	0.49	8.64	6.46	2.33
CMSX-4 pt.6	4.77	0.92	7.28	9.92	53.90	0.78	0.00	4.38	10.83	7.22

A3: Chemical composition of sample 5.1
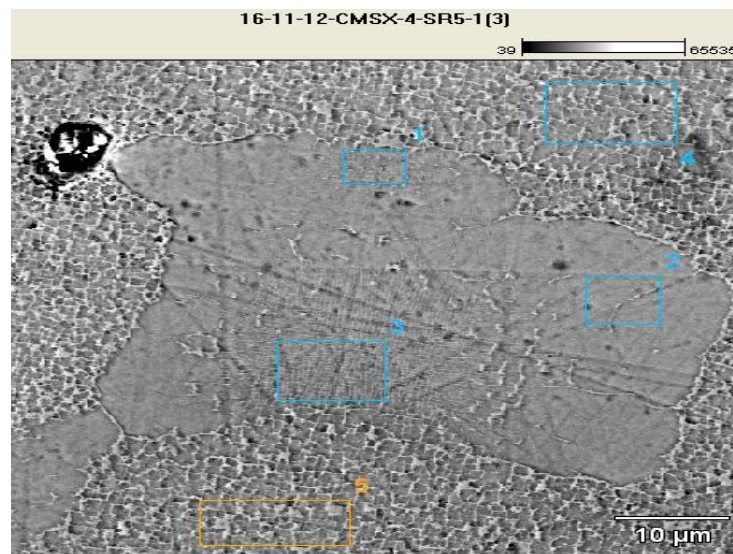
Accelerating Voltage: 20.0 kV

Magnification: 2000

16-11-12-CMSX-4-SR5-1(3)_pt2

```
30000
25000   Ni
        Co      Al
20000   Cr      Ta
        Ti      W
15000   Re      Re                                    Ni
        W       Hf   Mo                          W      Ta       Ta
10000   Mo           Ta                          Co   Re   Ni  Hf
        Ta      Ta   Re                           Hf   Co   W W
 5000   Hf      W    W              Ti Ti Cr Cr    Ta   Hf   Re      W
     0
        0         2         4         6         8
                              keV
```

16-11-12-CMSX-4-SR5-1(3)_pt3

```
25000       Ni
            Co      Al
20000       Cr      Ta
            Ti      W
15000       Mo      Re
                    Hf                            Ni      Ni
10000   Re          W                        W      Ni
        W       Ta  Re                       Co   Re   W    Ta
 5000   Ta      Hf  Ta                        Hf   Co   ReHf
        Hf      Hf  Mo           Ti Ti Cr Cr   Ta   Hf   W      W
     0
        0         2         4         6         8
                              keV
```

16-11-12-CMSX-4-SR5-1(3)_pt4

```
25000       Ni
            Co      Al
20000       Cr      Ta
            Ti      W
15000   Re          Re                            Ta
        Mo          Hf                        Ni      Ni
10000   W                                    W      W
        Hf      Ta                           Co   Re   Re
 5000   Ta      W    W                         Hf   Co   W    Ta
                Hf   Mo          Ti Ti Cr Cr    Ta   Hf   Hf  W
     0
        0         2         4         6         8
                              keV
```

16-11-12-CMSX-4-SR5-1(3)_pt5

```
25000       Ni
            Co      Al
20000       Cr      W
            Ti      Ta
15000   Mo          Re
        W           Hf                             Ni
10000   Re                                    Ni   Ta
        Hf      W                            W      W
 5000   Ta      Ta   W                        Co   Re   Re      W
                Hf   Mo          Ti Ti Cr Cr    Ta   Hf   W   Ta
     0                                                    Hf
        0         2         4         6         8
                              keV
```

81

A4:   Chemical compositions for sample 5.1 wt. %

	Al	Ti	Cr	Co	Ni	Mo	Hf	Ta	W	Re
CMSX-4 pt.1	7.39	1.89	4.44	7.65	63.93	0.61	0.00	11.17	4.51	1.41
CMSX-4 pt.2	7.68	2.11	3.38	7.31	61.87	0.54	1.79	13.42	1.90	0.00
CMSX-4 pt.3	7.10	1.81	5.62	8.83	61.97	0.72	0.11	7.97	4.01	0.86
CMSX-4 pt.4	6.17	1.39	6.31	9.11	58.20	0.94	1.21	9.26	5.16	2.25
CMSX-4 pt.5	6.41	1.13	7.11	9.53	59.36	0.62	0.00	8.11	5.83	1.91

A5:   Microstructure at eutectic region for different withdrawal rates

Sample 1.1 - eutectic region.
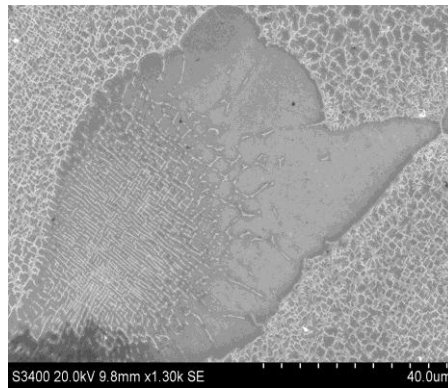
Sample 3.1 - eutectic region.
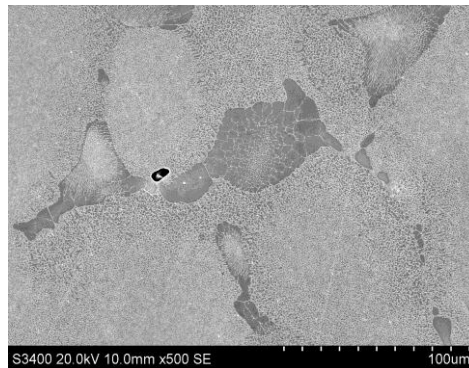
Sample 5.1 - eutectic region.
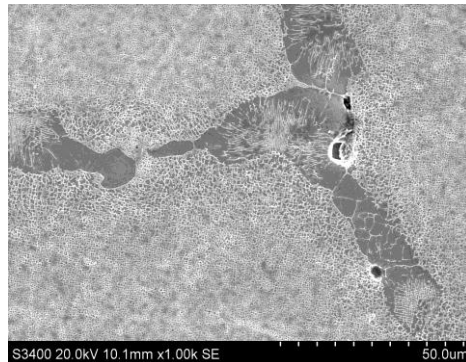
APPENDIX B: CREEP TESTS

B1:   For velocity 1 mm/min

Test report

1. Sample-Nb.	: P1/12/121/06	Material	: SX
2. Sample-Nb.	: RU-P1-651-121/12	Cast	: n/d
Number of detail	: 1.6 selector	Certification	: n/d
Set-Nb.	: n/d	Customer order no.	: rpa
		Lab order no.	: 121/12

Results

Machine	:	M1	Test	:	2
Temperature nom	:	982 [℃]	Stress max.	:	248.1 [MPa]
Temperature max.	:	983 [℃]	Force max.	:	4.85 [kN]

Duration total	:	85 [h]	37 [min]
Duration of test	:	82 [h]	37 [min]
Start	: 2012-11-27 10:49:04
End	: 2012-12-01 00:26:29
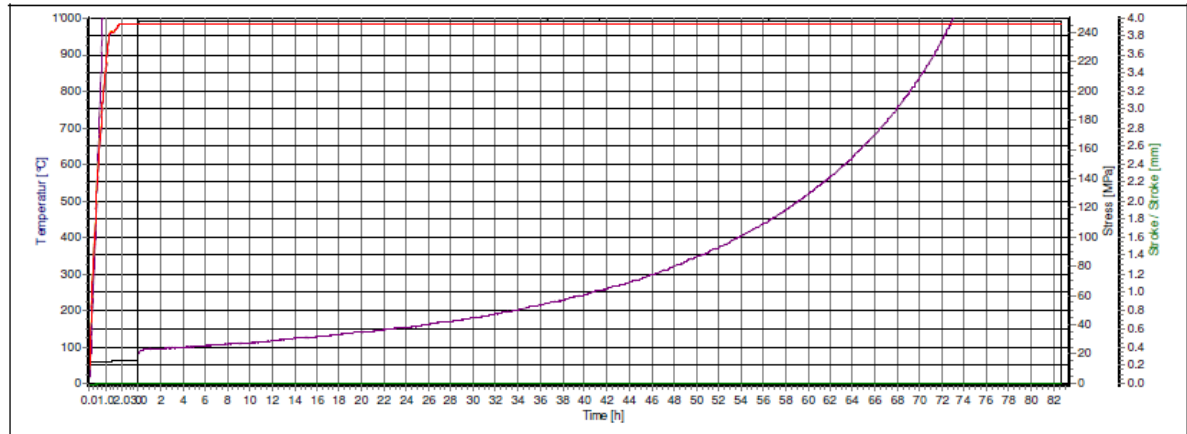
Test report

1. Sample-Nb.	: P1/12/121/05	Material	: SX
2. Sample-Nb.	: RU-P1-651-121/12	Cast	: n/d
Number of detail	: 1.6 selector	Certification	: n/d
Set-Nb.	: n/d	Customer order no.	: rpa
		Lab order no.	: 121/12

Results

Machine	:	M2	Test	:	2
Temperature nom	:	982 [℃]	Stress max.	:	248.1 [MPa]
Temperature max.	:	983 [℃]	Force max.	:	4.87 [kN]

Duration total	:	103 [h]	20 [min]
Duration of test	:	98 [h]	52 [min]
Start	: 27.11.2012 10:03:25
End	: 01.12.2012 17:23:18
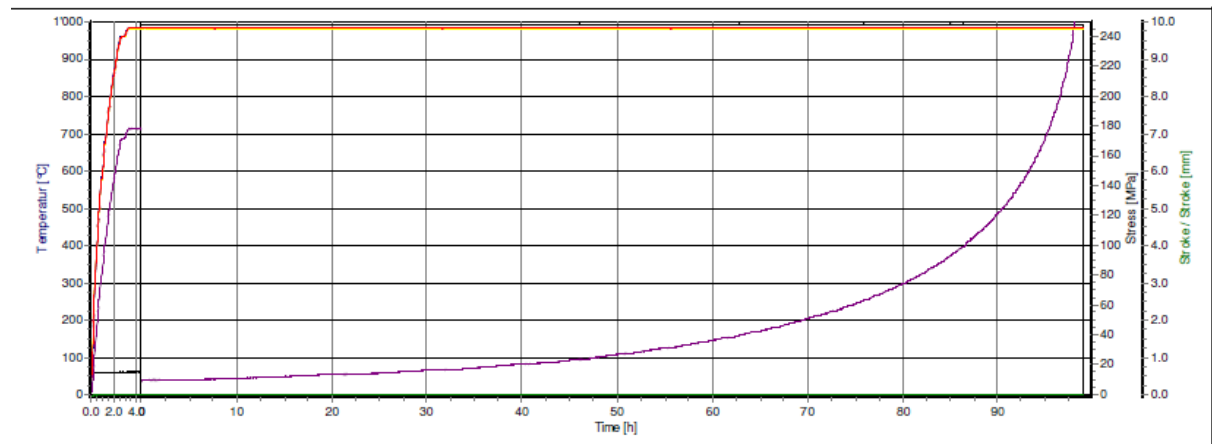
B2: For velocity 3 mm/min

Test report

1. Sample-Nb.	: P1/12/121/04	Material	: SX	Duration total	: 129 [h] 32 [min]
2. Sample-Nb.	: RU-P1-651-121/12	Cast	: n/d	Duration of test	: 126 [h] 52 [min]
Number of detail	: 3.6 selector	Certification	: n/d		
Set-Nb.	: n/d	Customer order no.	: rpa		
		Lab order no.	: 121/12		

Results

Machine	: M1	Test	: 4	Start	: 2012-11-20 14:13:11
Temperature nom	: 982 [°C]	Stress max.	: 248.1 [MPa]	End	: 2012-11-25 23:45:17
Temperature max.	: 986 [°C]	Force max.	: 4.89 [kN]		
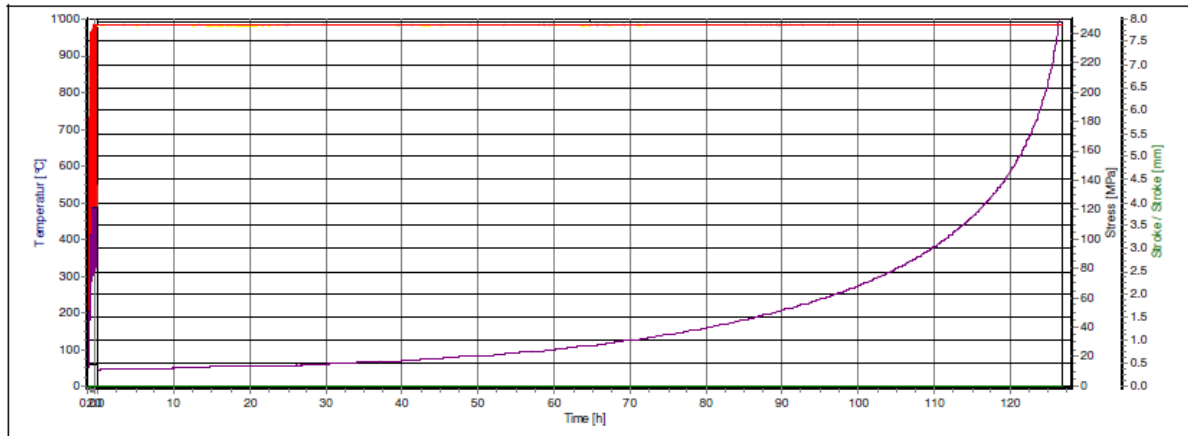
Test report

1. Sample-Nb.	: P1/12/121/03	Material	: SX	Duration total	: 119 [h] 24 [min]
2. Sample-Nb.	: RU-P1-651-121/12	Cast	: n/d	Duration of test	: 116 [h] 18 [min]
Number of detail	: 3.6 selector	Certification	: n/d		
Set-Nb.	: n/d	Customer order no.	: 121/12		
		Lab order no.	: rpa		

Results

Machine	: M1	Test	: 2	Start	: 2012-11-09 12:22:23
Temperature nom	: 982 [°C]	Stress max.	: 248.1 [MPa]	End	: 2012-11-14 11:46:27
Temperature max.	: 983 [°C]	Force max.	: 4.87 [kN]		

84
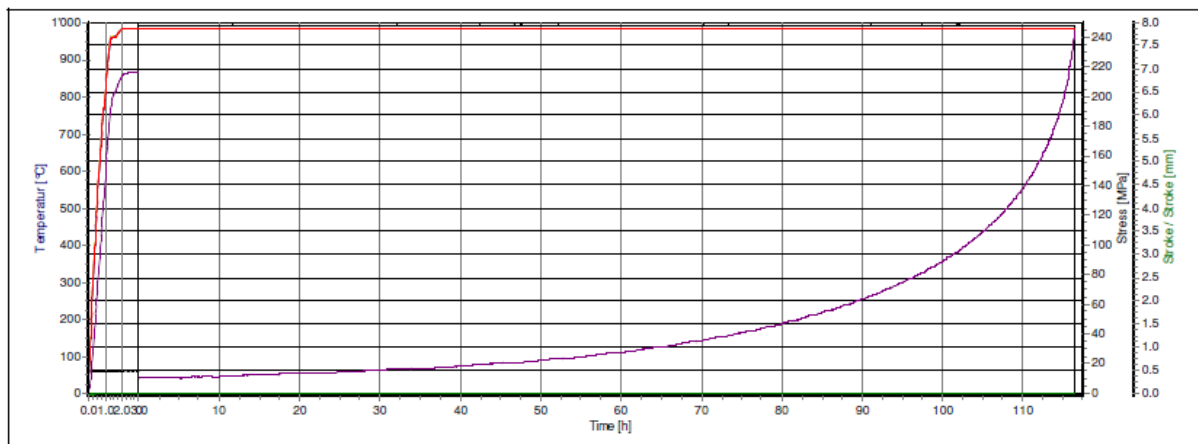
B3:   For velocity 5 mm/min

Test report

1. Sample-Nb.	: P1/12/121/02	Material	: SX	Duration total	:	106 [h] 54 [min]
2. Sample-Nb.	: RU-P1-651-121/12	Cast	: n/d	Duration of test	:	102] 34 [min]
Number of detail	: 5.6 selector	Certification	: n/d	Start	: 30.10.2012 19:32:09	
Set-Nb.	: n/d	Customer order no.	: rpa	End	: 04.11.2012 06:26:07	
		Lab order no.	: 121/12			

Results

Machine	: M2	Test	: 2		
Temperature nom	: 982 [°C]	Stress max.	: 248.1 [MPa]		
Temperature max.	: 991 [°C]	Force max.	: 4.87 [kN]		
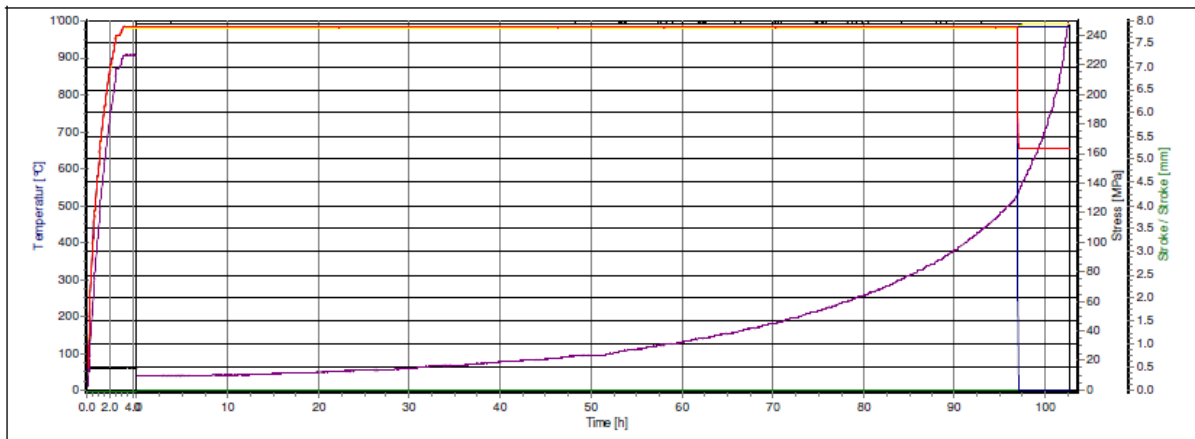
Test report

1. Sample-Nb.	: P1/12/121/01	Material	: SX	Duration total	:	121 [h] 26 [min]
2. Sample-Nb.	: RU-P1-651-121/12	Cast	: n/d	Duration of test	:	118] 58 [min]
Number of detail	: 5.6 selector	Certification	: n/d	Start	: 2012-10-30 20:13:58	
Set-Nb.	: n/d	Customer order no.	: rpa	End	: 2012-11-04 21:39:50	
		Lab order no.	: 121/12			

Results

Machine	: M1	Test	: 4		
Temperature nom	: 982 [°C]	Stress max.	: 248.1 [MPa]		
Temperature max.	: 985 [°C]	Force max.	: 4.87 [kN]		

85